Uniform Modal Frequencies and Damping in Multi-Legged Stewart Platforms

Yogesh Pratap Singh[*] and Ashitava Ghosal[†]

Abstract

This paper presents the design of a novel two-radii Gough–Stewart platform (TRGSP) for multi-axis vibration isolation with an arbitrary number of legs, capable of achieving uniform natural frequencies and damping across the first six degrees of freedom (DOF). Conventional single-radii Gough–Stewart platforms cannot achieve such uniform modal characteristics, limiting their effectiveness in six DOF isolation. The proposed TRGSP is dynamically isotropic with complete modal decoupling and enabling representation as six independent single-input-single-output dynamical systems, thereby simplifying damper tuning and controller design. For the first time, a general closed-form analytical framework is developed for dynamically isotropic TRGSPs with more than six legs, and all design variables are derived using a novel geometry-based approach that reduces the 3D dynamic isotropy problem to a 2D triangular geometry problem An innovative, cost-effective transitional design strategy is further proposed to upgrade existing platforms by adding legs to accommodate increased payloads while preserving dynamic isotropy. Under stated modeling assumptions, the analytical results are validated numerically through finite element method (FEM) simulations for multiple leg configurations and further confirmed experimentally using a 6-leg dynamically isotropic TRGSP prototype developed for spacecraft micro-vibration isolation. The framework provides a practical solution for next-generation multi-axis vibration isolation systems for use in spacecraft and precision applications.

Keywords: Vibration isolation, Damping, Natural frequency, Modal decoupling, Dynamic isotropy, Two-radii Gough–Stewart platform (TRGSP)

1 Introduction

Multi-axis vibration isolation technology is critical to ensure the high performance of precision equipment [1, 2, 3] because even small disturbances can propagate through the structure, degrading system's functionality [4, 5, 6, 7]. In spacecraft applications, these low-level vibrations or micro vibrations are generated by various disturbance sources, including flexible appendages, reaction wheels, momentum wheels, control moment gyroscopes, cyro-coolers, and other vibration devices [4, 5, 8, 9, 10]. These micro vibrations degrade the functionality of sensitive optical payloads such as imagers or cameras, as well as other vibration-sensitive components such as inter-satellite communication links affixed to the spacecraft bus [5, 11]. The

---

[*] Department of Mechatronics, Indian Institute of Technology Bhilai, India. Email: yogeshsingh@iitbhilai.ac.in

[†] School of Engineering and Applied Science, Ahmedabad University, India. Corresponding author, Email: ashitava.ghosal@ahduni.edu.in

Hubble Space Telescope (with a 2.4 m aperture) requires a pointing stability of $0.007''$ and an attitude control accuracy of 0.025°, whereas the James Webb Space Telescope (with a 6.5 m aperture) requires a pointing stability of $0.004''$ and an attitude control accuracy of 0.001° [12, 13, 14], and in both telescopes, vibration isolation plays a key role in their effective functioning. A significant number of researchers have focused on Gough–Stewart platform (GSP)-based isolation systems [12, 15, 16, 17, 18, 19, 20, 21, 22] for these purposes.

A six degrees of freedom (DOF) GSP consists of a fixed base, a moving platform for mounting payloads, and six prismatic joints or dampers-based legs connecting these platforms. Researchers have used GSPs both to locally isolate delicate and sensitive payloads [5, 7, 23] and to suppress disturbances from onboard sources such as reaction wheels [24, 25]. To achieve vibration control, a variety of approaches, such as passive [26, 27, 28, 29], semi-active [30, 31] and fully active control methods have been adopted. These active control methods have been implemented with different actuators such as voice coils [25, 32, 33, 34, 35, 36], electromagnetic actuators [33], piezoelectrics [37, 38, 39, 40], and magnetostrictive materials [41]. The choice between passive [26, 42, 43, 44, 45, 46], semi-active [47, 48, 49], active [50] or hybrid [51] systems depends strongly on mission requirements [1]. Passive damping can limit amplification near resonance but often compromises high-frequency attenuation. Active systems, on the other hand, can suppress resonance and provide a steep roll-off at higher frequencies. The drawback is the added complexity of control electronics, real-time computation, and the associated increase in mass and power demand—factors that are critical in spacecraft applications.

Recent advancements have significantly diversified vibration isolation strategies beyond conventional architectures with growing interest in machine-learning-optimized quasi-zero stiffness (QZS) metastructures, multi-step broadband QZS isolators, origami- and tunable-inspired mechanisms, and bio-inspired negative-stiffness metamaterials that provide adaptable stiffness – damping characteristics across wide frequency ranges [52, 53, 54, 55, 56, 57, 58, 59, 60, 61, 62, 63, 64, 65, 66, 67, 68]. These approaches have demonstrated substantial improvements in transmissibility curve slope and static–dynamic stiffness trade-offs, particularly for low-frequency isolation. Although QZS isolators utilizing negative-stiffness mechanisms substantially improve low-frequency vibration isolation, they are still restricted to single-axis motion and necessitate accurate nonlinear parameter calibration to prevent bistable behavior [69, 70, 71, 72, 73, 74, 75]. High-precision spacecraft payloads, however, require simultaneous vibration isolation in all six degrees of freedom. These nonlinear single DOF strategies [48, 76, 77, 78, 79, 80, 81] thus motivate the need for multi-axis architectures. There have been several attempts to employ alternative configurations of parallel mechanisms, but these designs are not generally adopted for multi-axis vibration isolation either due to practical limitations or because they provide vibration isolation in fewer than six DOFs [26, 82, 83, 84, 85]. In this context, GSP based architectures remain particularly compelling for multi-axis vibration isolation.

A conventional six-legged GSP cannot provide effective multi-axis vibration isolation because it cannot achieve uniform natural frequency and damping across the first six modes corresponding to the first six degrees of freedom [86, 87]. This shortcoming has led to the idea of *dynamic isotropy*, where the first six natural frequencies are made nearly equal [88, 89, 90, 91, 92, 93, 94]. Dynamic isotropy ensures that resonance peaks are aligned, preventing the isolation region of one mode from being disturbed by peaks from other cross modes [1]. The concept is effective and advantageous – the dynamic isotropy configuration can simplify damper tuning in passive vibration control, and identical dampers can be used on the legs of the GSP for the given frequency bandwidth. It also simplifies controller design in active systems due to decoupling of modes - an isotropic GSP can often be controlled as six independent single-input–single-output (SISO) systems, rather than a coupled multi-input–multi-output (MIMO) system [95, 96, 97], making use of decoupled control strategies. The lowest natural frequency also plays a key role in defining system stability [98], making isotropy even more valuable as it maximizes the lowest natural frequency. While other forms of isotropy—such as kinematic [99, 100, 101, 102], stiffness [103], and static isotropy [87, 104, 105] have been studied and are useful for applications requiring precise pointing [95], they are not sufficient for vibration isolation because the first six natural frequencies are not aligned. Unlike kinematic, stiffness and static isotropy, dynamic isotropy explicitly incorporates mass distribution, inertia, and stiffness properties, which makes it more suited to vibration problems. Recent studies show that enriched mass-matrix formulations, structural modeling choices, and ANN-based surrogate prediction significantly influence modal frequency and dynamic stiffness estimation in parallel mechanisms [106, 107, 108, 109].

In a conventional GSP, all the connection points lie on a single radius on both platforms, inherently limiting its dynamic behavior. A two-radii GSP (TRGSP) has been demonstrated to exhibit dynamic isotropy [90, 92, 110, 111]. In this configuration, joints are placed on two radii of each platform (see Fig. 1(a)). While these works have been insightful, studies on GSPs with more than six legs remain scarce [112, 113], and none have looked at the dynamic isotropy problem for TRGSPs with more than six legs. Having more struts or legs (¿ 6) can be useful in the following ways:

- It allows heavy loads to be distributed among several actuators, especially when individual actuator capacity is limited [113].
- It enables payload capacity upgrades without designing a new GSP. Instead of fabricating a new setup to meet updated launch requirements for heavier payloads, additional legs can be added to an existing system, reducing cost and build time while maintaining six DOF vibration isolation performance.
- Using more than six legs in a dynamically isotropic configuration could provide both uniform shock distribution and higher stability. By comparison, a conventional six-legged GSP designs are vulnerable to multi-directional shocks because the loads cannot be distributed evenly across all struts [114].

---

[1] A background discussion on modal coupling and the motivation for dynamic isotropy is provided in Appendix A.

Some multi-legged platforms are already in use– for example, the Airborne Laser system and the Active Rack Isolation System (ARIS) aboard the International Space Station (ISS) both employ eight-leg GSPs [113, 115]. They can retain full six-DOF functionality even if one or two legs fail. Other studies have considered eight-leg GSPs for shock isolation [114, 116, 117]. While Yong et al. [113] proposed orthogonal GSPs and extended them to even-legged platforms, their framework was meant for pointing accuracy, not vibration isolation, and does not address dynamic isotropy or odd-legged designs. Drawing on literature, the present work addresses these gaps and makes the following contributions:

- We propose a two-radii GSP (TRGSP) with an arbitrary number of legs that achieves uniform natural frequencies and damping for the first time to the best of our knowledge.
- A novel geometry-based framework is developed that yields closed-form solutions for dynamic isotropy conditions. This approach, valid for both even and odd numbers of legs, reduces the TRGSP design problem to a set of relationships involving triangles.
- We demonstrate decoupling of all six modes, enabling a complex MIMO system to be analyzed as six independent SISO systems, thereby simplifying multi-axis vibration isolation dynamic analysis.
- We show that multiple dynamic isotropic configurations are possible, allowing flexible designs that respect interference limits, dimensional constraints, and actuator/leg count.
- An innovative transitional design strategy is introduced, where existing TRGSP hardware can be upgraded by adding legs when payload demands increase. This makes the approach cost-effective because actuators or dampers are expensive. This transition is facilitated by our closed-form solution technique.
- Finally, isotropy in TRGSPs with more than six legs is validated using FEM simulations in ANSYS APDL and verified experimentally with a 6 legged TRGSP hardware prototype developed in collaboration with the Indian Space Research Organization (ISRO). The analytical model is calibrated against experimental modal characteristics, allowing for an accurate alignment between theory and prototype response.

While the primary focus is on achieving uniform damping and natural frequencies through dynamic isotropy, the framework remains flexible. The legs can be equipped with passive, semi-active, active, or hybrid isolation technologies to further enhance performance.

The remainder of this paper is organized as follows. Section 2 introduces the nomenclature and parameters related to the TRGSP employed in this study. These design parameters represent the radii, angular variables, and height parameters that define the connection or anchor points on a TRGSP, and the nomenclature remains consistent for TRGSPs with any number of legs. Section 3 presents the analytical framework and the novel geometry-based approach used to derive closed-form solutions for dynamically isotropic designs with an arbitrary number of legs. These closed-form expressions provide a generic framework for obtaining dynamically isotropic configurations for any chosen payload and any leg count. The parameters derived from the closed-form expressions result in a system with equal natural frequency associated with the first six DOFs and decouple the dynamic equations into six independent SISO systems. Section 4 addresses the design process and the practical considerations associated with TRGSPs. The methodology ensures that the mechanical design is both practical and feasible by keeping the selected parameters within spatial constraints and ensuring that the legs do not interfere with one another. Section 5 validates the analytical results using FEM simulations in various TRGSP configurations. An FE model consistent with the analytical assumptions is created in ANSYS for dynamically isotropic TRGSPs with different numbers of legs. The obtained frequency response functions (FRFs) demonstrate uniform natural frequency and damping along with mode decoupling, consistent with the analytical formulation. Section 6 proposes a cost-effective transitional design strategy across different TRGSP configurations while maintaining dynamic isotropy. This transition involves adding extra legs when the payload increases, enabling the use of a TRGSP with a larger number of legs to accommodate the enhanced load. This approach leverages the closed-form solution and requires modifying only the anchoring points rather than manufacturing an entirely new configuration for enhanced payload. Section 7 provides experimental validation using data from a six-leg TRGSP prototype. The FRF curves obtained experimentally exhibit uniform damping and natural frequency characteristics consistent with the analytical and FE results, thereby validating the general framework. A model-calibration is done to align analytical and prototype responses to minimize minor discrepancies. Finally, Section 8 summarizes and concludes the study while highlighting the significance of the work and outlining future directions.

2 Geometry of TRGSP

This section defines the geometric framework and notation used to describe two-radii Gough–Stewart platforms (TRGSPs). These design variables (radii, angular, and height parameters) influence natural frequencies and damping characteristics of the system and are essential to deriving the dynamic isotropy conditions discussed subsequently. As described in Section 1, TRGSP differs from the traditional GSP with the anchoring points located on two radii on each platform instead of one radius in a traditional GSP. In a TRGSP with more than six legs, the legs are organized into two distinct sets. Within each set, the legs are placed with rotational symmetry along the circumference.

Let n_1 denote the number of legs in the first set (from A_1 to B_1 in Fig. 1(a)). All legs in this set have the same length, and each successive leg is rotated by $\theta_1 = \frac{2\pi}{n_1}$. Similarly, the second set contains n_2 legs

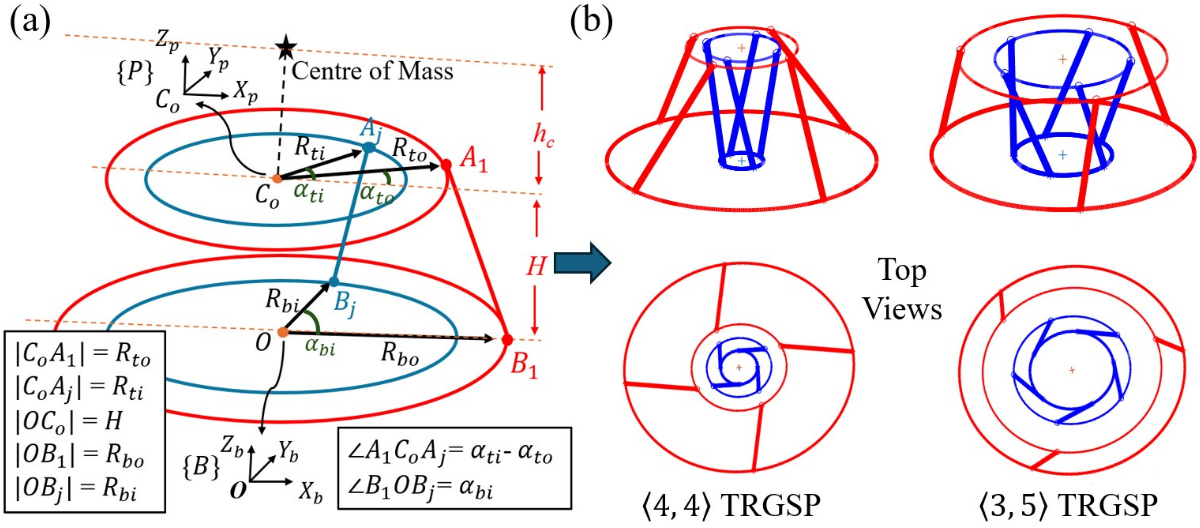

Figure 1: (a) Geometry of a two-radii GSP (TRGSP) in its neutral position showing how the two sets of legs are arranged on the inner and outer radii. (b) Representative of eight-leg TRGSP configurations, i.e., $\langle 4, 4\rangle$ and $\langle 3, 5\rangle$, and their corresponding top views depicting the resulting geometric differences between equal and unequal leg sets.

of equal length (from A_j to B_j in Fig. 1(a), with $j = n_1 + 1$), with each leg rotated by $\theta_2 = \frac{2\pi}{n_2}$. Thus, a TRGSP with $n = n_1 + n_2$ legs is denoted throughout this paper as $\langle n_1, n_2\rangle$. For example, a TRGSP with six legs can be written as $\langle 3, 3\rangle$, since it has three legs in each set, each arranged with a rotational symmetry of $\theta_1 = \theta_2 = 120°$. Similarly, Fig. 1(b) depicts two illustrative examples of eight-leg TRGSPs – the $\langle 4, 4\rangle$ configuration and $\langle 3, 5\rangle$ configuration. In the former, each radius supports four evenly spaced legs, while in the latter, the outer and inner radii accommodate three and five legs, respectively. The associated top-views clearly show how changing the number of legs in each set alters the angular spacing as well as the overall distribution of anchor points on the platform. These visualizations further highlight that both configurations maintain the capacity to attain DOF motion while providing distinct geometric and practical design alternatives. This geometric arrangement governs leg orientations and load distribution, which affects stiffness coupling between translational and rotational modes.

The anchor points A_1 to A_n on the mobile platform are distributed along two concentric radii, denoted by R_{ti} (inner) and R_{to} (outer), with C_o as the center. Similarly, the base platform anchor points B_1 to B_n are located on two radii, represented by R_{bi} (inner) and R_{bo} (outer), with O as the center. The notations shown in Fig. 1(a) correspond to the neutral configuration, in which the fixed frame $\{B\}$ and the moving frame $\{P\}$ are parallel to each other. The vertical distance between the mobile and base platforms in the neutral configuration is denoted by H. The variable h_c specifies the vertical offset of the payload's center of mass (COM) from the mobile platform. The coordinates expressed in the base frame $\{B\}$ are written as $\{x_b, y_b, z_b\}$, while those in the moving frame $\{P\}$ are represented as $\{x_p, y_p, z_p\}$. The reference vector

$\boldsymbol{OB_1}$, having magnitude R_{bo}, is aligned with the $\boldsymbol{X_b}$ axis. The angular parameters α_{bi}, α_{to}, and α_{ti} are defined as the angles subtended by vectors $\boldsymbol{OB_j}$, $\boldsymbol{C_oA_1}$, and $\boldsymbol{C_oA_j}$, respectively, with the $\boldsymbol{X_b}$ axis (refer to Fig. 1(a)). Each leg is connected to the mobile platform through a spherical joint and to the base platform through a spherical or universal joint.

For completeness, the anchor points illustrated in Fig. 1(a) are explicitly defined using the notation introduced above. The anchor points on the bottom outer platform $(B_1, \ldots, B_{n_1})$ expressed in the fixed frame $\{B\}$ are given by $\mathbf{B}_j = [R_{bo}\cos((j-1)\theta_1),\, R_{bo}\sin((j-1)\theta_1),\, 0]^T$, and the corresponding anchor points on the top outer platform $(A_1, \ldots, A_{n_1})$ expressed in the moving frame $\{P\}$ are given by $\mathbf{A}_j = [R_{to}\cos(\alpha_{to} + (j-1)\theta_1),\, R_{to}\sin(\alpha_{to} + (j-1)\theta_1),\, 0]^T$, where $j = 1, \ldots, n_1$. Similarly, the anchor points on the bottom inner platform $(B_{n_1+1}, \ldots, B_n)$ are defined as $\mathbf{B}_q = [R_{bi}\cos(\alpha_{bi} + (q - n_1 - 1)\theta_2),\, R_{bi}\sin(\alpha_{bi} + (q - n_1 - 1)\theta_2),\, 0]^T$, and the corresponding anchor points on the top inner platform are $\mathbf{A}_q = [R_{ti}\cos(\alpha_{ti} + (q - n_1 - 1)\theta_2),\, R_{ti}\sin(\alpha_{ti} + (q - n_1 - 1)\theta_2),\, 0]^T$, where $q = n_1 + 1, \ldots, n$. These expressions define the anchor locations for arbitrary $\langle n_1, n_2 \rangle$ configurations. For clarity, the legs belonging to the outer set $(j = 1, \ldots, n_1)$ connect the outer anchor points of the bottom and top platforms $(R_{bo} \rightarrow R_{to})$, while the legs in the inner set $(q = n_1 + 1, \ldots, n)$ connect the inner anchor points $(R_{bi} \rightarrow R_{ti})$. This configuration represents the nominal outer-outer and inner-inner leg TRGSP. However, feasible solutions may also occur for parameter regimes where $R_{bo} < R_{bi}$ and/or $R_{to} < R_{ti}$. In these cases, despite the reversal in the relative magnitudes of the radii, the leg connections remain associated with the same anchor sets, namely $(R_{bo} \rightarrow R_{to})$ and $(R_{bi} \rightarrow R_{ti})$.

The design variables R_{bo}, R_{to}, R_{bi}, R_{ti}, H, α_{to}, and $(\alpha_{bi} - \alpha_{ti})$ are determined such that the TRGSP achieves uniform natural frequency and damping. The methodology for this determination is presented in the next section.

3 Geometry-based analytical approach

This section develops the mathematical formulation that results in the closed-form solution using a novel geometry-based approach. The analytical approach involves determining the first six natural frequencies corresponding to the six degrees of freedom of the TRGSP. This requires finding the stiffness matrix $[\mathbf{K}_T]$ and the mass matrix $[\mathbf{M}]$ in the task space. Each leg is assumed to have the same axial stiffness k in its joint space. The force transformation matrix $[\mathbf{B}]$ [23, 40], which maps joint space forces to the task space or cartesian space forces, is employed to derive the stiffness matrix $[\mathbf{K}_T]$ in terms of the system's geometric parameters. Consequently, the stiffness matrix in the task space [40] can be expressed as

$$[\mathbf{K}_T]_{6\times 6} = k[\mathbf{B}][\mathbf{B}]^T \ , \tag{1}$$

where the force transformation matrix for the TRGSP with n legs is given by

$$[\mathbf{B}]_{6\times n} = \begin{bmatrix} \boldsymbol{s_1} & \cdots & \boldsymbol{s_n} \\ ({}^B[\mathbf{R}]_P({}^P\boldsymbol{p_1} - {}^P\boldsymbol{H_c})) \times \boldsymbol{s_1} & \cdots & ({}^B[\mathbf{R}]_P({}^P\boldsymbol{p_n} - {}^P\boldsymbol{H_c})) \times \boldsymbol{s_n} \end{bmatrix}. \tag{2}$$

In the above equation, $\boldsymbol{s_q} = \dfrac{{}^B\boldsymbol{t} +{}^B [\mathbf{R}]_P\, {}^P\boldsymbol{p_q} -{}^B \boldsymbol{b_q}}{l_q}$, $q = 1, \ldots, n$ and the vector ${}^P\boldsymbol{H_c}$ represents the location of the combined center of mass (COM) of the mobile platform and the payload with respect to the mobile platform. The vector $\boldsymbol{S}q$ $(= l_q\boldsymbol{s}_q)$ lies along the qth leg of the TRGSP, whose length is l_q. The symbol ${}^B\boldsymbol{t}$ denotes the vector from the center of the base platform to the center of the mobile platform. The quantities ${}^P\boldsymbol{p_q}$ and ${}^B\boldsymbol{b_q}$ specify the coordinates of the anchor points on the mobile and base platforms, expressed in their respective frames. In the neutral configuration, the two platforms remain parallel (so that rotation matrix ${}^B[\mathbf{R}]_P = [\mathbf{I}]$), and the payload's COM, the center of the mobile platform, and the center of the base are aligned along the same vertical line (i.e., ${}^B\boldsymbol{t} = [0\ 0\ H]^T$ and ${}^P\boldsymbol{H_c} = [0\ 0\ h_c]^T$). The analytical formulation is developed under the assumption that the TRGSP operates at this neutral configuration. This is reasonable for micro-vibration isolation and precise control applications, since the mobile platform experiences only small displacements. This motion is typically limited to sub-millimetre displacements (less than 0.1 mm, i.e., approximately 1–100 μm) and rotations below 0.5° [5, 13, 14]. Moreover, small deviations of the platform from the neutral or dynamically isotropic configuration may slightly affect the uniformity of the first six natural frequencies. A sensitivity analysis with respect to the design variables has been carried out and is presented in Section 7.2. At this position, the matrix $[\mathbf{B}]$ remains constant, although for a given $[\mathbf{B}]$, the connection points are not uniquely defined [93, 113], leading to multiple solutions.

The mass matrix $[\mathbf{M}]$ takes a diagonal form when the principal axes of the payload are aligned with the global coordinate system, and is expressed as

$$[\mathbf{M}]_{6\times 6} = \mathrm{diag}\,[\, m_p,\ m_p,\ m_p,\ I_{xx},\ I_{yy},\ I_{zz}] \,, \tag{3}$$

where m_p denotes the mass of the payload (including the mobile platform), and I_{xx}, I_{yy}, and I_{zz} are the principal moments of inertia about the $\boldsymbol{X}$, $\boldsymbol{Y}$, and $\boldsymbol{Z}$ axes with respect to the payload's COM. The mass and inertia of the legs are neglected, as they are expected to be negligible compared to the overall payload mass. The natural frequency matrix in the task space $[\mathbf{G}]$ can be derived using Eqs. (1), (2) and (3) and is expressed as

$$[\mathbf{G}]_{6\times 6} = [\mathbf{M}]^{-1}[\mathbf{K_T}] = [\mathbf{M}]^{-1}k[\mathbf{B}][\mathbf{B}]^T = \begin{bmatrix} \mathbf{P} & \mathbf{T} \\ \mathbf{T^T} & \mathbf{U} \end{bmatrix}, \tag{4}$$

with $[\mathbf{P}] = \mathrm{diag}(\ \lambda_1,\ \lambda_2,\ \lambda_3\ )$, $[\mathbf{U}] = \mathrm{diag}(\ \lambda_4,\ \lambda_5,\ \lambda_6\ )$, $[\mathbf{T}] = \begin{bmatrix} \mu_{11} & -\mu_{12} & 0 \\ \mu_{12} & \mu_{11} & 0 \\ 0 & 0 & \mu_{33} \end{bmatrix}$, where expressions of λ_i and μ_{ij} are given in the B [2].

The sub-matrices $[\mathbf{P}]$, $[\mathbf{U}]$, and $[\mathbf{T}]$ separate translational, rotational, and cross-coupling terms. Dynamic isotropy is achieved when the coupling matrix $[\mathbf{T}]$ vanishes and all the six diagonal terms become identical, leading to uniform natural frequencies across all six modes. The obtained matrix $[\mathbf{G}]$ is a function of leg count (n_1 and n_2), payload properties (from mass matrix), and all the design variables for an TRGSP, i.e., $R_{bo},\ R_{to},\ R_{bi},\ R_{ti},\ H,\ a,,\ (\alpha_{bi} - \alpha_{ti})$ and α_{to}. As can be observed, the term $(\alpha_{bi} - \alpha_{ti})$ effectively acts as a single design variable since it represents the relative angular offset of the legs connecting R_{bi} and R_{ti}. Therefore, the difference between these angles is the parameter of interest, while the absolute value of α_{ti} may be chosen arbitrarily to obtain multiple feasible configurations. The zero entries in the matrix $[\mathbf{G}]$ arise from the symmetry created by the equal angular spacing of legs of the same type. As stated, $\langle n_1,\ n_2\rangle$ TRGSP has two sets of legs with lengths l_{out} and l_{in} corresponding to the two radii on each platform. The expressions for these leg lengths using TRGSP design parameters are provided in B. The relationship between these two leg lengths is governed by the leg length ratio represented by a, thus

$$l_{in} = a\ l_{out}. \tag{5}$$

All six eigenvalues of the natural frequency matrix in Eq. (4) must be equal to obtain dynamic isotropic conditions and is given as

$$\lambda_1 = \lambda_2 = \lambda_3 = \lambda_4 = \lambda_5 = \lambda_6 = \omega^2 \text{ and } \mu_{11} = \mu_{12} = \mu_{33} = 0, \tag{6}$$

where ω is the natural frequency of the TRGSP and when μ_{ij} go to zero, λ_1 to λ_6 become the eigenvalues of the matrix $[\mathbf{G}]$. It can be observed from Eq. (6) that the variable λ_1, λ_2 and λ_3 corresponds to $\boldsymbol{X}$, $\boldsymbol{Y}$ and $\boldsymbol{Z}$ DOFs, while variable λ_4, λ_5 and λ_6 corresponds to Rot($\boldsymbol{X}$), Rot($\boldsymbol{Y}$) and Rot($\boldsymbol{Z}$) DOFs, respectively.

3.1 Development of closed-form solutions

To determine dynamically isotropic configurations analytically, the isotropy conditions in Eq. (6) are simplified to get geometrical observations. This subsection presents the step-by-step reduction of this observation into closed-form expressions using a novel geometry-based approach. Furthermore, the present closed-form dynamic isotropy formulation assumes an axisymmetric inertia distribution such that $I_{xx} = I_{yy}$. These conditions define the applicability domain of the analytical framework and are consistent with many practical spacecraft payload configurations.

A $\langle n_1,\ n_2\rangle$ TRGSP with uniform natural frequency and damping will depend on where and how the legs are mounted. The design involves finding unknown parameters from the known given parameters

---

[2] While the provided expression is simplified for clarity by considering $h_c = 0$ (no variation in the center of mass), it's important to highlight that we can easily incorporate the variable h_c as an input (as the payload is specified by us).

Table 1: Geometrical interpretations of a dynamically isotropic TRGSP with an arbitrary number of legs for the case of $h_c = 0$ (center of mass on the top platform).

Case	**Condition used**	**Simplified Equation**	**Geometrical Interpretation in Fig. 2(a)**
1	$\lambda_1 = \lambda_3$ and Eq. (5)	${b_i}^2 = R_{ti}^2 + R_{bi}^2 - 2R_{ti}R_{bi}\cos(\alpha_{bi} - \alpha_{ti})$	$\Delta Q_oP_1R_1$: triangle with sides R_{bi}, R_{ti} and b_i (cosine rule)
2	$\lambda_1 = \lambda_3$ and Eq. (5)	${b_o}^2 = R_{to}^2 + R_{bo}^2 - 2R_{to}R_{bo}\cos(\alpha_{to})$	$\Delta Q_oP_2R_2$: triangle with sides R_{bo}, R_{to} and b_o
3	$\mu_{11} = 0$	$R_{ti}R_{bi}\sin(\alpha_{bi} - \alpha_{ti}) = \frac{n_1a^2}{n_2} \times R_{to}R_{bo}\sin(\alpha_{to})$	Area of $\Delta Q_oP_1R_1 = \frac{n_1a^2}{n_2} \times$ (Area of $\Delta Q_oP_2R_2$)
4	$\mu_{12} = 0$	$R_{ti}(R_{ti} - R_{bi}\cos(\alpha_{bi} - \alpha_{ti})) = \frac{n_1a^2}{n_2} \times R_{to}(R_{bo}\cos(\alpha_{to}) - R_{to})$	$(\overline{Q_oR_1})P_{g1} = \frac{n_1a^2}{n_2} \times (\overline{Q_oR_2})P_{g2}$
5	$\mu_{12} = 0$ and $\mu_{11} = 0$	$\tan\theta_i = \tan\theta_o$	$\angle Q_oR_1P_1 = 180° - \angle Q_oR_2P_2 \Rightarrow \theta_i = \theta_o = \theta$
where $b_i = H\sqrt{C_1}$, $b_o = \frac{H\sqrt{C_2}}{a}$, $C_1 = \left(\frac{n_1(3a^2-1)+2n_2}{n_1+n_2}\right)$, $C_2 = \left(\frac{a^2(2n_1-n_2)+3n_2}{n_1+n_2}\right)$			

and free/input variables. The unknowns (design parameters) for a TRGSP are R_{bo}, R_{to}, R_{bi}, R_{ti}, H, α_{to}, and $(\alpha_{bi} - \alpha_{ti})$ and the free variables will be the number of legs in each set (n_1 and n_2) and leg length ratio (a) alongside the given parameters like payload's mass (m_p), inertia (I_{xx}, I_{yy}, I_{zz}), and COM height (h_c, which is assumed equal to zero for simplicity). In our formulations, the payload properties are expressed in ratios where K (the ratio I_{xx}/I_{zz}) and Q (the ratio I_{xx}/m_p). The necessary condition of $\lambda_4 = \lambda_5$ (refer to Eq. (6)) is practically valid for axisymmetric wheel-like payload ($I_{xx} = I_{yy}$).

Simplifications of dynamic isotropy conditions in Eq. (6) give rise to several useful geometrical observations, which can be seen in Table 1 and Fig. 2(a) (for case $h_c = 0$). If any set of geometries satisfies conditions in Table 1, the design parameters obtained will represent a dynamically isotropic configuration. Hence, a 3D dynamically isotropic TRGSP problem is simplified into a 2D triangle problem with this approach. The challenge to obtain the sides for any general triangles ($\Delta Q_oP_1R_1$) in Fig. 2(b) is overcome by obtaining sides of the corresponding right angle triangle $\Delta Q_oP_{1,r}R_1$ in Fig. 2(b) (denoted by subscript 'r' for right angle case).

To obtain analytical closed-form solutions for this right-angle triangle case in Fig. 2(b), we make use of Pythagoras' theorem in $\Delta Q_oP_{1,r}R_1$. Let $R_{ti,r} = x\ H_r$, where x is a constant scaling $R_{ti,r}$ and H_r then

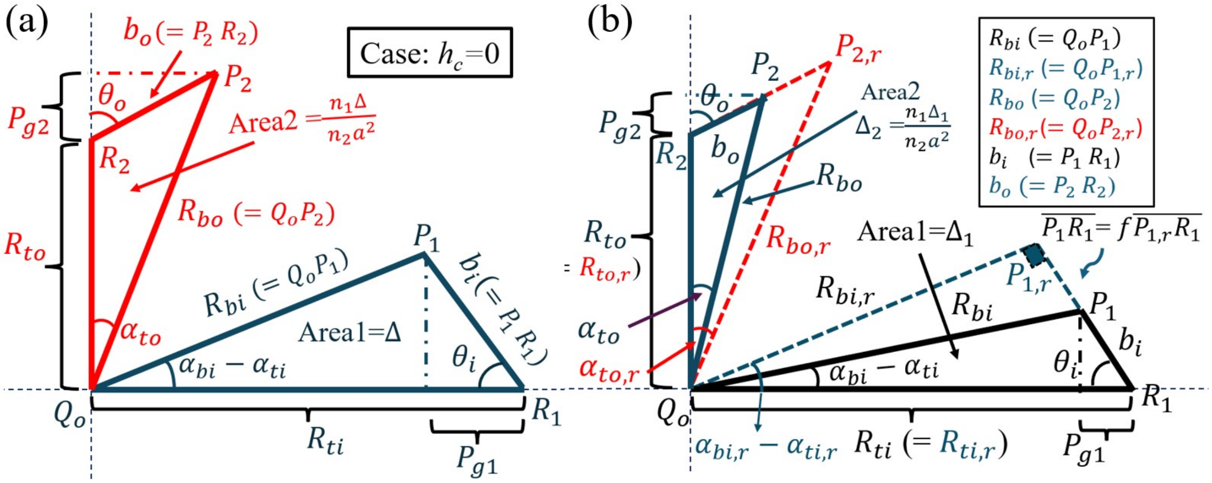

Figure 2: (a) Geometrical interpretation of the dynamic isotropy condition in Table 1, reducing the dynamically isotropic TRGSP problem into sets of triangles ($\Delta Q_o P_1 R_1$ and $\Delta Q_o P_2 R_2$). (b) A general triangle ($\Delta Q_o P_1 R_1$) can be obtained by using the corresponding right-angled triangle ($\Delta Q_o P_{1,r} R_1$) to derive different TRGSP configurations.

$$\begin{gathered} R_{bi,r} = \sqrt{\left(x^2 H_r^2 - b_{ir}^2\right)} = \sqrt{(x^2 - C_1)}\ H_r\ , \\ \sin\left(\alpha_{bi,r} - \alpha_{ti,r}\right) = \frac{b_{ir}}{x\ H_r} = \frac{\sqrt{C_1}}{x}\ , \end{gathered} \tag{7}$$

where $b_{ir} = H_r \sqrt{C_1}$ and value of C_1 and C_2 are given in Table 1. Using the condition $\lambda_4 = \lambda_5 = \lambda_6,\ \mu_{11} = 0$ (see expressions in B) and Eq. (5), on simplification, we get

$$R_{to,r} = \sqrt{\frac{1}{n_1 a^2}\left\{\frac{2 n_2^2 K C_1}{a^2}\left(\frac{a^2}{n_2} + \frac{1}{n_1}\right)(x^2 - C_1) - n_2 x^2\right\}}\ H_r. \tag{8}$$

Using the condition $\lambda_1 = \lambda_2 = \lambda_3,\ \mu_{12} = 0$ (see expressions in B) and Eq. (5) on simplification, we get

$$R_{bo,r} = \sqrt{\frac{1}{n_1 a^2}\left\{n_1 a^2 R_{to,r}^2 + n_2 C_1 H_r^2 + 2 H_r^2 (n_1 a^2 + n_2)\right\}}\ . \tag{9}$$

From the condition of $\mu_{11} = 0$, and Eq. (5), we get

$$\sin\left(\alpha_{to,r}\right) = \frac{n_2 R_{bi,r} R_{ti,r}\ \sin\left(\alpha_{bi,r} - \alpha_{ti,r}\right)}{n_1\ a^2\ R_{bo,r} R_{to,r}}\ . \tag{10}$$

Using the expressions for the variables obtained and the trigonometry identity $\sin^2\left(\alpha_{to,r}\right) + \cos^2\left(\alpha_{to,r}\right) = 1$ in $\mu_{11} = 0,\ \mu_{12} = 0$, and on simplification, we get

$$x = \sqrt{\frac{K\left(\frac{a^2(2n_1 - n_2)+3n_2}{(n_1+n_2)}\right)\left(\frac{(n_1(3a^2-1)+2n_2)}{(n_1+n_2)}\right)^2}{K\left(\frac{a^2(2n_1 - n_2)+3n_2}{(n_1+n_2)}\right)\left(\frac{(n_1(3a^2-1)+2n_2)}{(n_1+n_2)}\right) - a^2}} = \sqrt{\frac{K\ C_2\ {C_1}^2}{K\ C_1\ C_2 - a^2}}\ , \tag{11}$$

where C_1 and C_2 are function of free/input variable a, n_1 and n_2 and their values are given in Table 1. Using $\lambda_3 = \lambda_4$ and on simplification, we obtain the expression for H_r in its explicit form as

$$\begin{aligned} H_r &= \sqrt{\frac{Qn_1\left(K\left(\frac{a^2(2n_1-n_2)+3n_2}{(n_1+n_2)}\right)\left(\frac{(n_1(3a^2\ -1)+2n_2)}{(n_1+n_2)}\right) - a^2\right)}{\left\{Kn_2\left(\frac{(n_1(3a^2-1)+2n_2)}{(n_1+n_2)}\right)^2\right\}}} \\ &= \sqrt{\frac{Qn_1(KC_1C_2 - a^2)}{Kn_2\ C_1^2}}. \end{aligned} \tag{12}$$

Using values of x and H_r in Eqs. (7), (8), (9)and (10), we get design variable for right angle triangle case ($\Delta Q_oP_{1,r}R_1$ and $\Delta Q_oP_{2.r}R_2$ in Fig. 2(b)), we get

$$\begin{aligned} &R_{ti,r} = \sqrt{\frac{n_1\ QC_2}{n_2}}, R_{to,r} = \frac{1}{a}\sqrt{\frac{n_2\ QC_1}{n_1}}, R_{bi,r} = \sqrt{\frac{n_1\ Qa^2}{n_2\ KC_1}}\ , \\ &\theta = \arctan\left(\frac{a}{\sqrt{KC_1C_2 - a^2}}\right) \text{ and } (\alpha_{bi,r} - \alpha_{ti,r}) = 90^\circ - \theta, \\ &R_{bo,r} = \sqrt{\frac{n_2\ QC_1}{n_1a^2} + \frac{Q(KC_1C_2 - a^2)}{a^2K{C_1}^2}\left(C_1 + \frac{2n_1a^2}{n_2} + 2\right)}, \end{aligned} \tag{13}$$

where the leg length ratio a, number of legs n_1 and n_2 can be taken as input (free variable) with K and Q as known variable. The geometries, i.e., $\Delta Q_oP_{1,r}R_1$ and $\Delta Q_oP_{2,r}R_2$ shown in Fig. 2(b) can be constructed from the known results in Eq. (13) above. The variable $\theta_i = \theta$ denotes the angle between the sides P_1R_1 and Q_oR_1, while $\theta_o = \theta$ denotes the angle between the sides P_2R_2 and Q_oR_2. These angles are of practical importance, as their values remain unchanged during the scaling/perturbation operation introduced subsequently.

Now, these geometries are perturbed to generate the new geometries, i.e., $\Delta Q_oP_1R_1$ and $\Delta Q_oP_2R_2$ as shown in Fig. 2(b). The perturbations done along line $\overline{P_{1,r}R_1}$ will keep the leg length ratio a constant. This means such perturbations along line $\overline{P_{1,r}R_1}$ to generate $\overline{P_1R_1}$ (hence $\Delta Q_oP_1R_1$) also keeps design variables such as $R_{ti}(= R_{ti,r})$, $R_{to}(= R_{to,r})$ and θ_i & $\theta_o = \theta$ the same. Different a values generate new sets of triangles corresponding to their respective right-angled triangle. The new height H for the general triangle case ($\Delta Q_oP_1R_1$ and $\Delta Q_oP_2R_2$) will now be given as $H = fH_r$ (see Eq. (12)) because $\overline{P_1R_1} = f\ \overline{P_{1,r}R_1}$ (their lengths are directly proportional to H, see Fig. 2(b)), where f is a ratio (free variable) whose value could be less than 1, equal to 1 (right-angle case as in Eq. (13)) or greater than 1 (extension of line) depending on the design values we want for a TRGSP.

For intuitive understanding and proof of the perturbation concept, consider a perturbation where the side $P_{1,r}R_1$ in Fig 2(b) (equal to b_{ir} for right angle case) is scaled by a factor f. Thus, under this perturbation, the new variable $b_i = f\ b_{ir}$ is also scaled by the same factor f. Since b_i is a linear function of the height parameter H ($b_i = H\sqrt{C_1}$), the height H is correspondingly scaled by f. Consequently, b_o is also scaled by the same ratio ($b_o = H\sqrt{C_2}/a$). Because the geometry still forms a valid triangle, the first two cases in Table 1 remain satisfied with the same base radii R_{ti} and R_{to}. Furthermore, for fixed values of R_{ti} and R_{to}, identical angles $\theta_i = \theta_o = \theta$, and preserved ratios of b_i and b_o, the ratio of heights of the two new triangles after scaling in Fig 2(b) remain unchanged. This leads to identical triangle area ratio between two new triangles and therefore preserves the condition for the case 3 in Table 1 before and after the perturbation. Similarly, the ratio of P_{g1} and P_{g2} in Fig. 2(b) remains unchanged under the scaling, thereby satisfying the condition in case 4 of the table as well. It is important to note that this scaling physically corresponds to changing the platform height and determining different dynamically isotropic configurations for a given TRGSP height and the parameter a.

Interestingly, the new triangles due to scaling ($\Delta Q_oP_1R_1$ and $\Delta Q_oP_2R_2$) satisfy all the isotropic/geometric conditions in Table 1 and represents a dynamically isotropic design. The design variables for the general case ($R_{bi},\ \alpha_{bi} - \alpha_{ti}, R_{bo},\ \alpha_{to}$) which are different from the right-angled triangle case can be computed analytically in terms of ratios f, a, n_1, n_2 and payload properties (K, Q). This can be done by making use of geometrical relations in Fig. 2(b) using known variables (R_{ti}, R_{to}, θ_i and θ_o) and the new value of H. If H_r is the height of the platform for the right-angle triangle case and b_i, b_o represent sides of any general triangles in Fig. 2 with values given in Table 1, the general solution can be obtained as

$$\begin{aligned}
&H = f\ H_r\ ,\\
&R_{bi} = \sqrt{(R_{ti} - b_i\cos\theta_i)^2 + (b_i\sin\theta_i)^2}\ ,\\
&R_{bo} = \sqrt{(R_{to} + b_o\cos\theta_o)^2 + (b_o\sin\theta_o)^2}\ ,\\
&\alpha_{bi} - \alpha_{ti} = \arctan\left(\frac{b_i\ \sin(\theta_i)}{R_{ti} -\ b_i\cos(\theta_i)}\right)\ ,\\
&\alpha_{to} = \arctan\left(\frac{b_o\ \sin(\theta_o)}{R_{to} +\ b_o\cos(\theta_o)}\right)\ .
\end{aligned} \tag{14}$$

The above equations can be directly used to design a dynamically isotropic TRGSP with any number of legs.

It should be noted that the geometric construction summarized in Table 1 is derived under the assumption $h_c = 0$, same stiffness in each leg, legs are massless, and for axisymmetric inertia distribution. The relations listed in Table 1 are obtained by enforcing a subset of the isotropy conditions in Eq. (6) together with the leg-length ratio constraint $l_{in} = a\, l_{out}$. Under the assumed symmetry of the $\langle n_1, n_2 \rangle$ TRGSP configuration, these relations are sufficient to satisfy the remaining isotropy equalities, thereby ensuring full dynamic isotropy of the system. The construction also implicitly requires that the geometric parameters yield a real and non-degenerate triangular configuration, and from Eq.(12), we find that $C_1\ C_2 > a^2$. This imposes feasibility conditions on (n_1, n_2, a) and the associated geometric constants C_1 and C_2.

3.2 Dynamically isotropic natural frequencies

In this subsection, we derive the closed-form expression for dynamically isotropic natural frequency. Once the closed-form expressions for the design parameters are obtained, the corresponding natural frequencies can be written explicitly. For dynamic isotropy, all the natural frequencies ω (square root of the eigenvalues of $[\mathbf{G}]$ matrix) must be equal, i.e., $\lambda_1 = \lambda_2 = \lambda_3 = \lambda_4 = \lambda_5 = \lambda_6 = \omega^2$. It can be written in closed form after substituting the values of all the design parameters as

$$\omega_1 = \omega_2 = \omega_3 = \omega_4 = \omega_5 = \omega_6 = \omega = \sqrt{\frac{k(n_1 + n_2)}{3m_p}}\ . \tag{15}$$

Therefore, we get a uniform natural frequency for all six modes, which is independent of the specific TRGSP geometry. It should be noted that this holds only under the modeling assumptions adopted in this work, including identical axial stiffness in each leg, negligible leg inertia, linearization about the neutral configuration, and an axisymmetric payload inertia distribution.

3.3 Decoupling and damping in TRGSP

This subsection demonstrates that the resulting dynamically isotropic system can be reduced to six independent SISO systems with identical damping characteristics. Having established uniform natural frequencies across the first six DOFs, we now analyze how dynamic isotropy influences modal coupling and damping behavior. The dynamic equation of a TRGSP [95] under free vibration is expressed as

$$\ddot{\boldsymbol{X}} + [\mathbf{M}]^{-1}[\mathbf{C}_T]\ \dot{\boldsymbol{X}} + [\mathbf{M}]^{-1}[\mathbf{K}_T]\ \boldsymbol{X} = 0\ , \tag{16}$$

where $\mathbf{X} = [X; Y; Z; \mathrm{Rot}(X); \mathrm{Rot}(Y); \mathrm{Rot}(Z)]$[3].

Similar to Eq. (1), the damping matrix $[\mathbf{C}_T]$ can be represented in task space as $c[\mathbf{B}][\mathbf{B}]^T$, with c being the damping constant along each leg. Accurate prediction of the damping value in theory is challenging–typically requiring experimental determination. Although approaches such as Rayleigh damping are possible, we focus here on structural (hysteretic) damping, consistent with our prototype. For a linear hysteretic

---

[3] $\mathrm{Rot}(X),\ \mathrm{Rot}(Y)$ and $\mathrm{Rot}(Z)$ denote three rotational degrees of freedom about X, Y and Z axis, respectively.

material subjected to uniaxial loading, the loss factor (η) is stress-independent and can be treated as a material constant. An equivalent viscous damping representation can be derived using a single-degree-of-freedom Kelvin–Voigt model [111], giving the equivalent damping constant as $c = k\eta/\omega_e$, where ω_e is the excitation frequency. Accordingly, for a dynamically isotropic design, Eq. (16) reduces to six identical single-DOF systems of the form,

$$\ddot{x} + \frac{\eta}{\omega_e}\,\omega^2\,\dot{x} + \omega^2\,x = 0, \tag{17}$$

demonstrating that damping is uniformly distributed across all directions and the first six modes corresponding to the first six DOFs are decoupled. At resonance, the loss factor η and equivalent viscous damping ratio ζ are related by $\zeta = \eta/2$. The validation of all these results will be presented in Section 5.

Note that in practice, the excitation frequency ω_e is selected near the dominant vibration frequency of interest, which for vibration isolation applications typically corresponds to the natural frequency of the system. Since the dynamically isotropic configuration ensures that the first six natural frequencies are identical, the same effective value of ω_e applies to all directions. Consequently, the resulting equivalent viscous damping coefficients are also identical, leading to the uniform damping property observed in the reduced single DOF representation. In the FEM model later discussed in Section 5, this equivalence is implemented through constant structural damping assigned to each leg, corresponding to the same effective damping level predicted by the analytical formulation.

4 Design of $\langle n_1,\ n_2\rangle$ TRGSP with uniform natural frequency and damping

This section discusses the closed-form solution for designing a $\langle n_1,\ n_2\rangle$ TRGSP with uniform natural frequency and damping under the following overall considerations:

- **Practical design**: Ensures that the chosen parameters remain within the available spatial constraints, which is particularly critical in spacecraft applications.
- **Feasible design**: Guarantees that the legs do not intersect or interfere with one another in three-dimensional space.
- **Natural frequency consideration**: The dynamically isotropic natural frequency sets the threshold that marks the onset of the region of isolation.

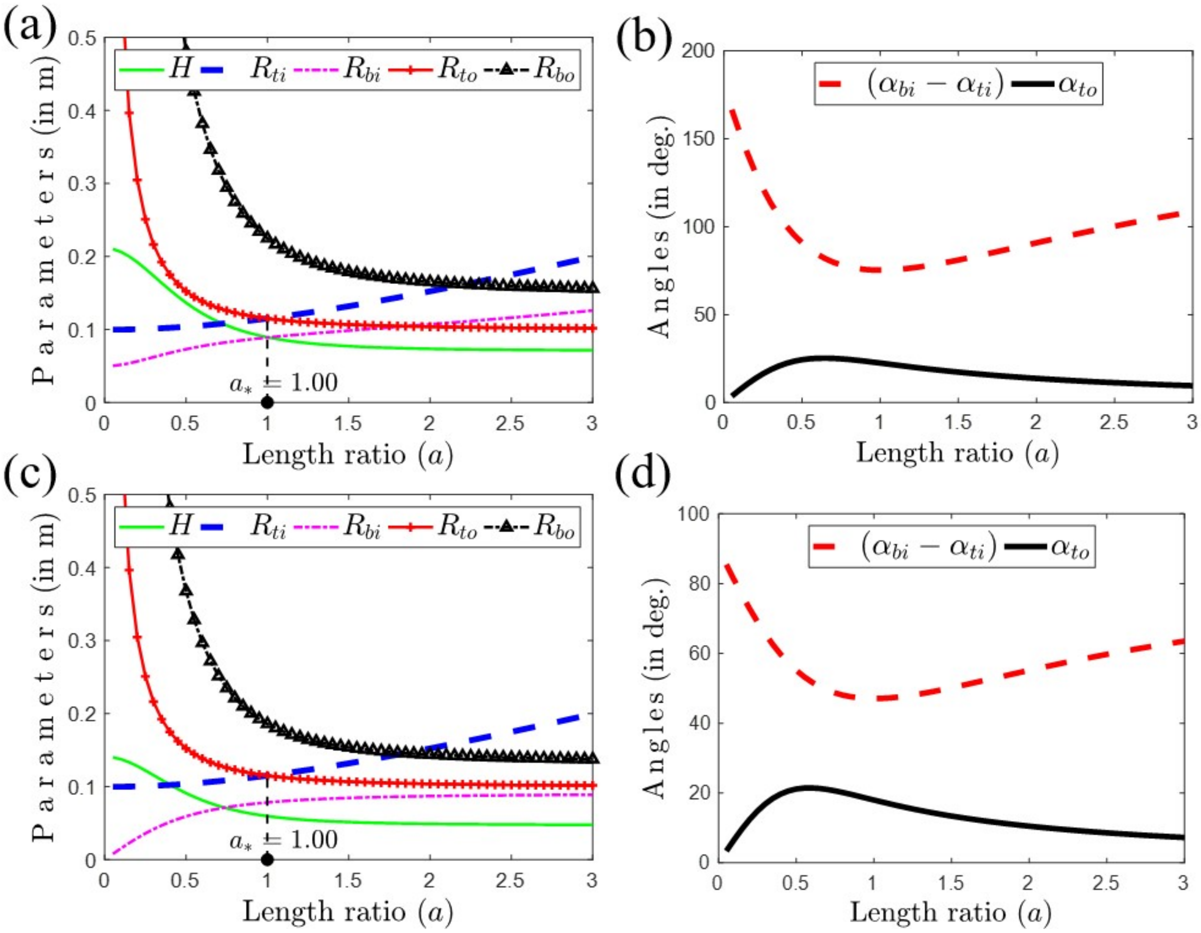

Figure 3: Variation of design parameters for dynamically isotropic $\langle n_1,\ n_2 \rangle$ TRGSPs with an equal number of legs in each set ($n_1 = n_2$, for e.g., $\langle 3,\ 3 \rangle$, $\langle 4,\ 4 \rangle$, $\langle 5,\ 5 \rangle$), (a) Variation of radii and height parameters for $n_1 = n_2$ with f=1.5, (b) Variation of angle parameters for $n_1 = n_2$ with f=1.5, (c) Variation of radii and height parameters for $n_1 = n_2$ with f=1.0, (d) Variation of angle parameters for $n_1 = n_2$ with f=1.0. For $K = 0.5390,\ Q = 6.63 \times 10^{-3}\ \text{m}^2,\ m_p = 10\ \text{kg},\ \text{and}\ k = 1.9 \times 10^5$ N/m.

4.1 Practical design

In this subsection, we will discuss the variation of design parameters with the number of legs and chosen free variables. This will ensure that the chosen parameters remain within the available spatial constraints, which is particularly critical in spacecraft applications. A very interesting observation that can be made for a class of TRGSP with $n_1 = n_2$ (equal numbers of legs in both the set, such as $\langle 3,\ 3 \rangle$, $\langle 4,\ 4 \rangle$, $\langle 5,\ 5 \rangle$) is that all the geometric parameters remain invariant with n_1 or n_2. This means that when we put $n_1 = n_2$, the expression for design variables becomes independent of n_1 and n_2. It is evident from the closed-form expressions for design variables in Eqs. (12), (13) and (14), which remain the same for this class. Hence, a TRGSP with $n_1 = n_2$ will have all design parameters the same for the given payload and input variable

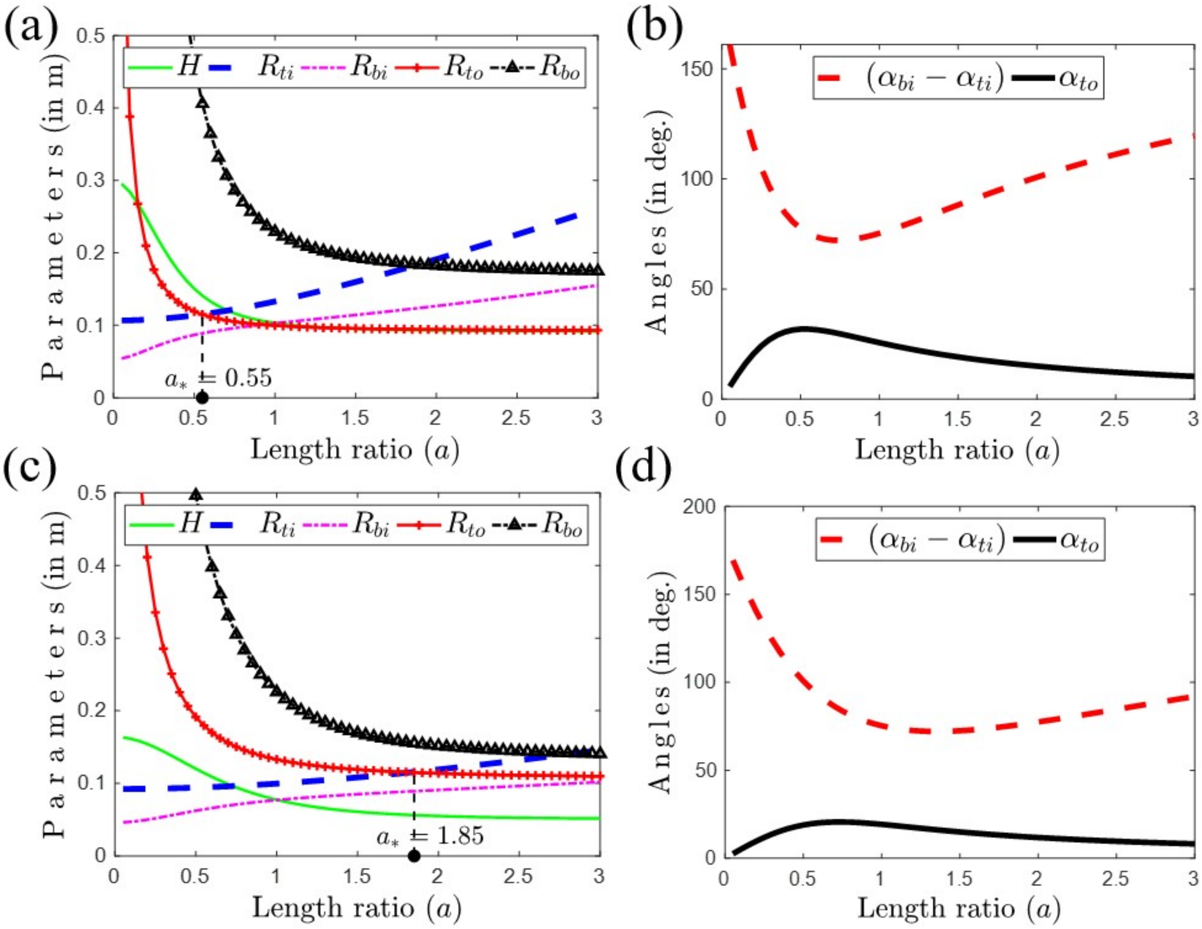

Figure 4: Variation of parameters for seven legged dynamically isotropic TRGSP where $n_1 \neq n_2$ for $f = 1.5$, (a) Variation of height and radii parameters for $\langle 4,\ 3\rangle$ TRGSP, (b) Variation of angle parameters for $\langle 4,\ 3\rangle$ TRGSP, (c) Variation of height and radii parameters for $\langle 3,\ 4\rangle$ TRGSP, (d) Variation of angle parameters for $\langle 3,\ 4\rangle$ TRGSP.

except the rotation angle of legs' anchoring points θ_1 and θ_2 ($\theta_1 = \frac{2\pi}{n_1}$ and $\theta_2 = \frac{2\pi}{n_2}$) that depend on the number of legs. Figure 3 shows the variation of parameters for a TRGSP with $n_1 = n_2$ for a typical payload of 10 kg. The properties considered are $I_{xx} = I_{yy} = 0.0663\ \text{kg}\cdot\text{m}^2,\ I_{zz} = 0.1230\ \text{kg}\cdot\text{m}^2$ ($K = 0.5390,$ and $Q = 6.63 \times 10^{-3}\ \text{m}^2$), $m_p = 10\ \text{kg},$ and $k = 1.9 \times 10^5$ N/m.

When the design variables are plotted for configurations such as $\langle 3, 3\rangle$, $\langle 4, 4\rangle$, or $\langle 5, 5\rangle$, the parameter values corresponding to a given value of the scaling variable f remain identical. Figure 3 illustrates this variation for two different values of f, i.e., $f = 1$ and $f = 1.5$. The case $f = 1$ in Fig. 3(c) corresponds to the right-angle triangle configuration discussed earlier in Fig. 2(b), whereas scaling the side length by a factor of 1.5 ($f = 1.5$) produces the set of design variables shown in Fig. 3(a). It can be observed that the platform height H scales by the same factor of 1.5, as expected, while the design parameters R_{ti} and R_{to}

remain unchanged after scaling, consistent with the closed-form solution. The remaining design parameters adjust accordingly to satisfy the dynamically isotropic conditions.

If $n_1 \neq n_2$, the TRGSPs will have different values of parameters depending on the value of n_1 and n_2. Figure 4 shows plots for one such case with seven leg TRGSP with $\langle 4, 3\rangle$ and $\langle 3, 4\rangle$ configurations for the same 10 kg payload. The design parameters in the above cases vary despite the same total number of legs and input parameters, due to different angular spacings between the two sets ($\theta_1 \neq \theta_2$) inherently altering the geometric conditions when $n_1 \neq n_2$.

Hence, the parameter variation curves can be generated for different values of the free variables f and a, and the appropriate solutions may be chosen based on space or dimensional constraints.

4.2 Feasible design

In this subsection, we will see how the feasibility of a design can be ensured before selecting a configuration to avoid leg interference from two different sets in 3D space. This can be addressed in two ways:

- **During the design stage:** Understanding the transition point (a_*) helps in preventing leg interference without the need for additional validation. This aspect will be discussed in detail in the subsequent subsection.

- **In the final stages:** If interference occurs even after the design is finalized, the relative angles ($\alpha_{bi} - \alpha_{ti}$) can play a crucial role. By utilizing the free choice of the variable α_{ti}, the connection points can be rotated while maintaining the difference of angles as constant for an isotropic configuration. It is to be noted that the design variable is ($\alpha_{bi} - \alpha_{ti}$) in our case, where the choice of α_{ti} is arbitrary. The variable ($\alpha_{bi} - \alpha_{ti}$) remains constant as before when α_{ti} and α_{bi} are changed by the same amount (angles). This means that the relative angular position of anchor points associated with variables R_{ti} and R_{bi} are the same, but this leads to a relative rotation between the two sets of legs and can help avoid interference without losing dynamic isotropy, as all the design variables are the same as before.

The presented feasibility approaches will ensure that the theoretically admissible designs remain mechanically realizable, as a dynamic isotropic configuration solution may be prone to leg collisions or unfavorable actuator orientations.

4.2.1 Configuration transition point (a_*)

Figure 3 shows an interesting observation that at $a = 1$, the two radii on the mobile platform coincide, i.e., $R_{to} = R_{ti}$. Thus, TRGSPs with all legs of equal length ($a = 1$) and equal number of legs in each set ($n_1 = n_2$) satisfy $R_{to} = R_{ti}$ in their dynamically isotropic configuration (with $h_c = 0$) for any value of f. This point also defines the configuration transition (a_*):

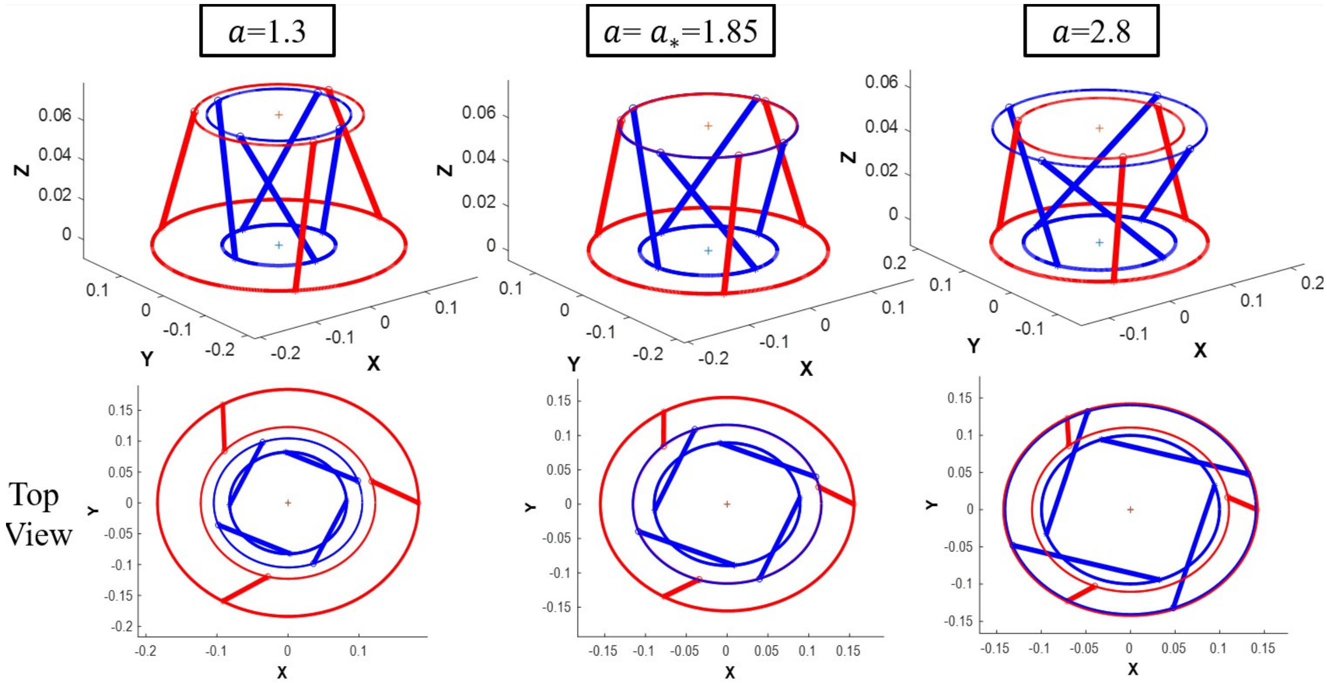

Figure 5: Configuration transition for ⟨3, 4⟩ TRGSP ($n_1 \neq n_2$) with top views; when $a < 1.3$, there is an outer-to-outer radius type leg connection; at $a = 1.3$, both the top radii merge, and $a > 1.3$, there is an outer-to-inner radius type leg connection.

- $a < a_*$: outer-to-outer and inner-to-inner radius connections.
- $a = a_*$: $R_{to} = R_{ti}$ – both top radii merge.
- $a > a_*$: outer-to-inner radius connections (cross-leg type).

The closed-form expression for a_* is given by

$$a_* = \sqrt{\frac{n_2(2n_2 - n_1)}{n_1(2n_1 - n_2)}} \ . \tag{18}$$

For $n_1 = n_2$, $a_* = 1$ and for $n_1 \neq n_2$, a_* varies – but are independent of payload properties. For instance, ⟨3, 4⟩ TRGSP has $a_* = 1.85$ (refer to Figs. 4(c) and 5). Similarly, ⟨4, 3⟩ TRGSP has $a_* = 0.55$ (refer to Figs. 4(a)). When $n_2 > 2n_1$ or $n_1 > 2n_2$, a_* does not exist, though other isotropic configurations remain possible for these cases. All TRGSP designs with $a < a_*$ are *mechanically feasible*, as the legs can never interfere in 3D space and are always safe to be utilized. However, designs with $a > a_*$ require a feasibility check. The radius at a_* depends only on payload properties and is given as

$$R_{to} = R_{ti} = \sqrt{2Q} \ . \tag{19}$$

Table 2: Comparison of analytical and FEM natural frequencies for different TRGSP configurations.

TRGSP configurations		Natural Frequencies (Hz)	DII
$\langle 3, 3\rangle$	FE	30.688, 30.720, 30.740, 30.963, 31.012, 31.042	1.010
	Analytical	31.025, 31.025, 31.025, 31.025, 31.025, 31.025	1.00
$\langle 4, 3\rangle$	FE	33.127, 33.193, 33.225, 33.457, 33.486, 33.512	1.011
	Analytical	33.512, 33.512, 33.512, 33.512, 33.512, 33.512	1.00
$\langle 4, 4\rangle$	FE	35.368, 35.421, 35.440, 35.735, 35.815, 35.838	1.013
	Analytical	35.825, 35.825, 35.825, 35.825, 35.825, 35.825	1.00

4.3 Natural frequency consideration

In this subsection, we will discuss how the dynamically isotropic natural frequency (ω), as derived in Section 3.2, is a key design consideration. This is because the isolation region begins at $\sqrt{2}\,\omega$, where the payload or reaction wheel is intended to operate. The natural frequency depends on the total number of legs ($n_1 + n_2$) (refer to Eq. (15)), so for a given k and m_p, a $\langle n_1,\ n_2\rangle$ TRGSP with more legs will exhibit a higher natural frequency for the first six modes. For instance, $\langle 3,\ 4\rangle$ and $\langle 4,\ 3\rangle$ dynamically isotropic TRGSPs have the same natural frequency despite differing design parameters as seen in Fig. 4. Interestingly, TRGSPs with $n_1 = n_2$ (equal numbers of legs in both the set such as ($\langle 3,\ 3\rangle$, $\langle 4,\ 4\rangle$, $\langle 5,\ 5\rangle$) have distinct dynamically isotropic natural frequencies as compared to each other even when all other design parameters are identical as seen in Fig. 3 (where the number of legs are different).

A $\langle 3,\ 3\rangle$ (6-leg) dynamically isotropic TRGSP exhibits the lowest natural frequency among this class for the same axial stiffness. However, for heavier payloads, increasing the number of legs may be necessary due to actuator load limits or the maximum load capacity on which the dampers are designed. The next section validates all these results and observations.

5 Validation using FEM model

In this section, we develop an FEM model using standard refined FEM tools ANSYS® to verify the appropriateness of our assumptions and analytical model. The FE model was developed such that the assumptions remained the same as those employed in the analytical formulation, thereby facilitating a direct comparison of natural frequencies, damping, and modal decoupling characteristics. The validation results are presented in this section, while the detailed modeling procedure, element type definitions, and the FE model configuration are provided in C, along with the corresponding FE model (refer to Fig. 10(a)).

5.1 Validation of uniform natural frequency

This subsection evaluates whether the first six natural frequencies corresponding to the first six DOFs obtained from FE simulations align with the closed-form analytical results for dynamically isotropic TRGSP configurations. FEM results for a $\langle 3,\ 3\rangle$, $\langle 4,\ 4\rangle$ and $\langle 4,\ 3\rangle$ dynamically isotropic TRGSPs are listed in Table 2. The closed-form solutions and simulation results are obtained for a typical payload of mass $m_p = 10$ kg, $I_{xx} = I_{yy} = 0.0663\ \text{kg}\cdot\text{m}^2$, $I_{zz} = 0.1230\ \text{kg}\cdot\text{m}^2$ ($K = 0.5390,$ and $Q = 6.63\times10^{-3}\ \text{m}^2$), $k = 1.9\times 10^5$ N/m, and free input variables $a = 1.3$ and $f = 1.5$. These three configurations were selected because they represent the smallest symmetric case ($\langle 3,\ 3\rangle$), an asymmetric case ($\langle 4,\ 3\rangle$), and the next symmetric case ($\langle 4,\ 4\rangle$), allowing us to verify that all the observations and results from analytical formulation remain valid across different dynamically isotropic geometric configurations and for any number of legs. The same design parameters (radii, angles and height) are applied for $\langle 3,\ 3\rangle$ and $\langle 4,\ 4\rangle$ ($n_1 = n_2$) in the FE model as derived in the closed-form analysis with only the change in their rotation angle. We evaluated the Dynamic Isotropy Index (DII), defined as the ratio of the largest to the smallest natural frequency (ideally close to one). The FEM results for all dynamically isotropic TRGSPs show close agreement with the closed-form solution results derived in Section 3.2 ($\omega = \sqrt{\frac{k(n_1+n_2)}{3m_p}}$), thereby validating our analytical approach for designing TRGSPs with arbitrary leg configurations and having uniform first six natural frequencies.

5.2 Validation of uniform damping

In this subsection, we verify that the uniform damping characteristics derived from the analytical model match the damping behavior observed in the FE based FRF results. All parts are assumed to be made of Aluminum alloy 2024, which inherently provides structural damping. Each leg assembly is given an equivalent viscous damping of $\zeta = 2\%$ (in the joint space), consistent with standard values for continuous metal structures. The steady-state dynamics of the TRGSP were studied by exciting the base platform nodes with unit displacement in all DOFs (rotations or translations one by one), respectively. The frequency response function (FRF) curves represent the relationship between the response of the payload's COM and the excitations applied at the base platform.

The FRF curve of the dynamically isotropic TRGSP with a 10 kg payload is shown in Fig. 6(a), where the three translational modes along $\boldsymbol{X}$, $\boldsymbol{Y}$, and $\boldsymbol{Z}$ are observed to overlap each other. Using the half-power bandwidth method, it is evident that damping is uniformly distributed across the three translational axes,

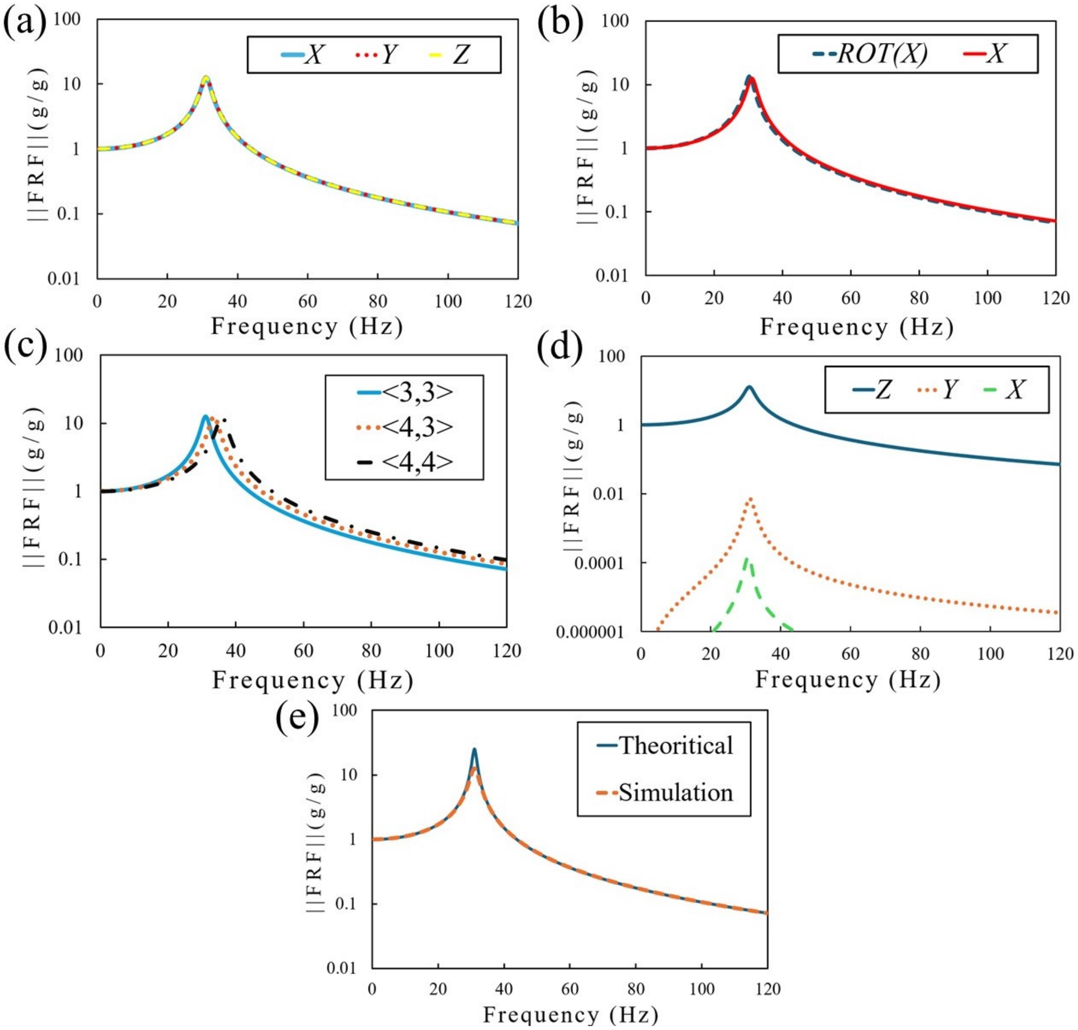

Figure 6: FRF plots for dynamically isotropic $\langle 3,\ 3\rangle$ TRGSP – (a) overlapping of the $\boldsymbol{X}$, $\boldsymbol{Y}$ and $\boldsymbol{Z}$ modes, (b) comparing the $\boldsymbol{X}$ and ROT($\boldsymbol{X}$) modes, (c) comparing $\boldsymbol{X}$ mode in $\langle 3,\ 3\rangle$, $\langle 4,\ 3\rangle$ and $\langle 4,\ 4\rangle$ TRGSP, (d) decoupling when only $\boldsymbol{Z}$ mode is excited, (e) comparison of results for $\boldsymbol{X}$ mode obtained using simulation in FEM and analytical model.

as discussed in Section 3.3. A similar trend is observed for the three rotational modes, and a comparison between the translational and rotational FRF curves can be seen in Fig. 6(b). Overall, the system shows an equivalent viscous damping of about $\zeta = 2.01$ % (loss factor $\eta = 4.02$ %) and a slope of $\simeq$ -16.72 dB/octave at the beginning of the region of isolation for the first six modes based on inputs validating dynamic isotropy and uniform damping.

Similarly, for the same payload and stiffness values ($m_p = 10$ kg and $k = 1.9 \times 10^5$ N/m), the resonance peaks of the $\langle 3,\ 3\rangle$, $\langle 4,\ 4\rangle$, and $\langle 4,\ 3\rangle$ dynamically isotropic TRGSPs are shown in Fig. 6(c), consistent with the natural frequency results in Table 2. For a given $\langle n_1,\ n_2\rangle$ configuration, all six DOF peaks overlap perfectly in the dynamically isotropic case. A comparison of slope and damping across different TRGSP configurations for the same given input is summarized in Table 3.

Table 3: Comparison of slope and damping for different TRGSP configurations.

Configuration	$\langle 3,3\rangle$	$\langle 4,3\rangle$	$\langle 4,4\rangle$
Slope during region of isolation(in dB/octave)	-16.72	-16.73	-16.77
Equivalent viscous damping (ζ in %)	2.01	1.87	2.08

5.3 Validation of decoupling

This subsection examines the extent of cross-DOF coupling by exciting individual modes and observing whether non-excited DOF responses remain negligible, thus validating modal decoupling. As discussed in Section 3.3, a dynamically isotropic TRGSP can be modeled as six independent SISO systems, achieving decoupling across the first six modes corresponding to the first six DOFs. This implies minimal or negligible cross-DOF interference when a particular DOF mode is excited– demonstrating decoupled behavior. For instance, Fig. 6(d) shows the FRF when only the translational mode along the $\boldsymbol{Z}$ axis is excited and the cross-mode responses remain comparatively negligible—an essential feature for simplifying controller design for active vibration control application. The peak cross-axis response relative to the primary excitation corresponds to coupling levels of approximately -65 dB (Z–Y) and -99 dB (Z–X), indicating that the cross-responses are several orders of magnitude smaller than the primary response and confirming strong modal decoupling of the dynamically isotropic configuration. In contrast, conventional GSPs exhibit significant surge–pitch and roll–sway cross-coupling.

5.4 Validation of damping model

This subsection validates the proposed analytical damping model with FEM simulation results for dynamically isotropic TRGSP. The damping model introduced in Section 3.3, based on a single DOF Kelvin–Voigt formulation, provides results that closely match the simulation outcomes across any $\langle n_1,\ n_2\rangle$ dynamically isotropic TRGSP configurations for a given loss factor η. As shown in Fig. 6(e), the $\boldsymbol{X}$ mode displays a strong agreement between the FEM simulation and the analytical model. Similar consistency is observed for other modes and for any $\langle n_1,\ n_2\rangle$ dynamically isotropic TRGSP configuration, thereby validating the proposed theoretical model. The small discrepancy is due to the step size selection, as properties change sharply across the resonance peak.

While FEM analysis provides an effective tool for verifying the dynamic behavior of a dynamically isotropic TRGSP, the analytical formulation developed in this work offers several advantages for design purposes. The closed-form expressions directly relate payload properties and geometric parameters to the conditions required for dynamic isotropy, allowing feasible configurations to be obtained without iterative numerical optimization. In addition, the analytical model provides physical insight into the influence of design parameters on natural frequencies, modal decoupling, and damping behavior, while FEM simulations are used primarily to verify the analytically derived configurations.

6 Transition between different $\langle n_1,\ n_2\rangle$ dynamically isotropic TRGSP designs

While the significance of dynamic isotropy for any $\langle n_1,\ n_2\rangle$ TRGSP has been discussed in the Introduction (Section 1), it must be emphasized that dynamic isotropy is meant only for a specific payload. This section addresses this limitation and outlines a cost-effective transition strategy when the payload changes.

As highlighted in the introduction, the advantage of TRGSPs with more than six legs becomes evident for heavier payloads, especially when the designed dampers or existing actuators cannot sustain the increased load. For instance, consider a payload increase from 10 kg to 13 kg with different inertia properties. Assume that a 6-leg $\langle 3,\ 3\rangle$ dynamically isotropic TRGSP has already been designed for the 10 kg case. Two possible approaches are possible to maintain dynamic isotropy: (i) design a new 6-leg $\langle 3,\ 3\rangle$ dynamically isotropic TRGSP with stiffer legs and dampers for passive vibration control, or upgrade to actuators of higher load capacity for active vibration isolation; or (ii) adopt a more cost-effective strategy by reusing the existing legs, fabricating one or two additional identical legs, and simply modifying the mounting points to restore dynamic isotropy.

During this transition, the key point to note is that l_{out} and l_{in} remain constant—implying that a is fixed according to Eq. (5). Our closed-form solution facilitates this transition process as it is based on the input variable a, that remains constant between two designs. The free variable f can be adjusted to enable this transition, since the payload properties are specified or fixed for the two designs. The leg length l_{out} for dynamically isotropic $\langle n_1,\ n_2\rangle$ TRGSP is expressed as

$$l_{\text{out}} = \frac{fH_r}{a}\sqrt{\frac{3a^2n_1+3n_2}{n_1+n_2}}\ . \tag{20}$$

For a transition design (denoted by the subscript t) with a different $\langle n_1,\ n_2\rangle$ configuration but the same a and l_{out}, the relation becomes

$$l_{\text{out},t} = \frac{f_tH_{r,t}}{a}\sqrt{\frac{3a^2n_{1t}+3n_{2t}}{n_{1t}+n_{2t}}}\ . \tag{21}$$

Hence, to achieve a valid transition, the value of f_t must be determined such that

$$l_{\text{out}} = l_{\text{out},t}\ . \tag{22}$$

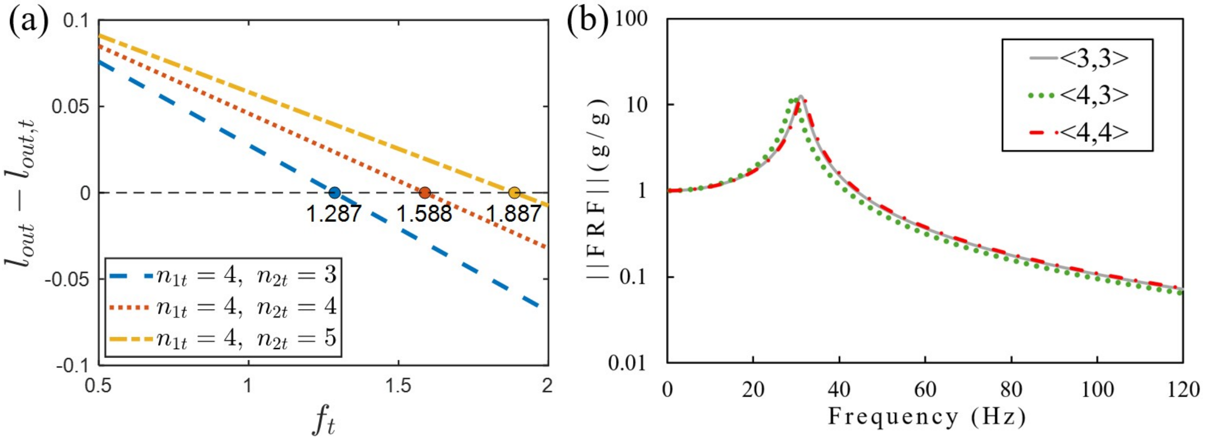

Figure 7: (a) Value of f_t when transitioning from 6-legged TRGSP (f=1.5) to 7-, 8-, and 9-legged dynamically isotropic TRGSP, (b) FRF curve for $\boldsymbol{X}$ mode for $\langle 3,\ 3\rangle$ (m_p= 10 kg), $\langle 4,\ 3\rangle$ (m_p= 13 kg) and $\langle 4,\ 3\rangle$ TRGSP (m_p= 13 kg) involved in the transition corresponding to Table 4.

To continue using legs of an existing dynamically isotropic $\langle 3,\ 3\rangle$ TRGSP (designed for a 10 kg payload) with a heavier payload of 13 kg, with properties: $m_p = 13$ kg, $I_{xx} = I_{yy} = 0.0792\ \mathrm{kg\cdot m^2}$, $I_{zz} = 0.1523\ \mathrm{kg\cdot m^2}$, we consider a seven-leg or eight-leg TRGSP. By applying Eq. (22), we can calculate the value of f_t that maintains the same leg length, and the results are shown in Fig. 7(a) and the transitional designs are summarized in Table 4. From the design parameters, it is evident that maintaining dynamic isotropy when transitioning from a $\langle 3, 3\rangle$ TRGSP to a $\langle 4, 3\rangle$ or $\langle 4, 4\rangle$ TRGSP requires only adjusting the connection points, which is significantly cheaper as compared to replacing the entire leg.

The FRF curves for the $\langle 3, 3\rangle$, $\langle 4, 3\rangle$, and $\langle 4, 4\rangle$ TRGSPs are shown in Fig. 7(b). It can be observed that although the number of legs increases, the natural frequency of the dynamically isotropic TRGSP decreases slightly for $\langle 4, 3\rangle$ and remains comparable for $\langle 4, 4\rangle$ relative to $\langle 3, 3\rangle$ TRGSP, and can also be seen in the last row of Table 4. This indicates that the region of vibration isolation is not compromised, as it begins around $\sqrt{2}\,\omega$, providing a similar scope for vibration isolation even with an increased number of legs due to the enhanced mass.

It should be noted that the direction and magnitude of the natural frequency shift are governed by Eq. (15). As the number of legs increases, the effective stiffness contribution in task space increases accordingly. This stiffness increase competes with the corresponding increase in mass of the system. Consequently, the ratio $k(n_1{+}n_2)/(3m_p)$ becomes the key parameter determining how the natural frequency varies with changes in both the number of legs and the effective system mass with each leg of the same stiffness.

Considering center of mass variation (h_c)

In the above discussions, the center of mass height from the top platform is not considered, as including

Table 4: Design variables for different TRGSP configurations– $\langle 3,\ 3\rangle$ (m_p= 10 kg), $\langle 4,\ 3\rangle$ (m_p= 13 kg) and $\langle 4,\ 3\rangle$ TRGSP (m_p= 13 kg).

Variable	$\langle 3,\ 3\rangle$	$\langle 4,\ 3\rangle$	$\langle 4,\ 4\rangle$
m_p (in kg)	10	13	13
I_{xx} (in $\text{kg}\cdot\text{m}^2$)	0.0663	0.0792	0.0792
I_{zz} (in $\text{kg}\cdot\text{m}^2$)	0.1230	0.1523	0.1523
k (in N/m)	1.9×10^5	1.9×10^5	1.9×10^5
a	1.3	1.3	1.3
f	1.5	1.287	1.588
H (in m)	0.0803	0.0789	0.0803
R_{bi} (in m)	0.0950	0.0963	0.0960
R_{bo} (in m)	0.1905	0.1773	0.1857
R_{to} (in m)	0.1091	0.0928	0.1046
R_{ti} (in m)	0.1247	0.1423	0.1195
$\alpha_{bi}-\alpha_{ti}$ (in deg.)	77.8153	69.2155	80.1655
α_{to} (in deg.)	19.2415	20.2283	20.1378
l_{out} (in m)	0.1241	0.1241	0.1241
l_{in} (in m)	0.1613	0.1613	0.1613
ω (Hz)	**31.025**	**29.391**	**31.421**

it complicates intuitive understanding. However, in practical applications, this effect is inevitable and can be easily incorporated into Eq. (2) for an axisymmetric payload by setting $\boldsymbol{H_c} = [0\ 0\ h_c]^T$, which introduces an additional known variable h_c into the closed-form solution. While this adds complexity, the overall observations remain unchanged, including the dynamically isotropic natural frequency. The geometry-based approach discussion in Section 3 also remains the same, except sides of the triangle will now be affected by the variable h_c. Although the complete formulation and process required to incorporate the additional known input variable h_c is lengthy and mathematically involved, the main steps that lead to the corresponding closed-form solution are outlined below.

- We include $\boldsymbol{H_c} = [0\ 0\ h_c]^T$ in Eqs. (4) and (6), where h_c is treated as a known design parameter.
- The overall dynamic isotropy problem is reduced to a pair of triangles, but the value of each side now incorporates the additional known variable h_c, similar to Fig. 2(a). The major difference with respect to the previous case is that here $\theta_i \neq \theta_o$.
- Similar to the case for $h_c = 0$, using Pythagoras theorem in $\Delta Q_o P_{1,r} R_1$ (refer to Fig. 2(b)), we get all the variables for the right-angle triangle case as a function of payload properties (including h_c), number of legs (n_1, n_2) and variable a.
- Similar to the previous case, when $h_c = 0$, we scale a right-angle triangle to a general triangle using the free variable f, and obtain a general triangle pair to get a closed-form solution.

Table 5: Comparison of natural frequencies of TRGSP obtained via analytical (A), FEM (F), and experiment (E), along with experimental setup and damping extraction methods.

Mode	**A (Hz)**	**F (Hz)**	**E (Hz)**	**Experimental setup**	**Damping extraction method**
$\boldsymbol{X}$	30.46	29.49	28.75	Base fixed on slip table, excited with sine sweep (0.5 g, 5–500 Hz), tri-axial accelerometers.	Half-power bandwidth (frequency domain).
$\boldsymbol{Y}$	30.46	29.51	29.00	Same as $\boldsymbol{X}$ mode.	Half-power bandwidth.
$\boldsymbol{Z}$	30.46	29.65	29.25	Mounted on 4-ton LDS shaker, sine sweep (0.5 g, 5–500 Hz), tri-axial accelerometers.	Half-power bandwidth.
Rot. $\boldsymbol{X}$	30.46	30.70	29.49	Impact hammer test (Kistler 9722A500), two accelerometers on diametric ends.	Logarithmic decrement (time domain).
Rot. $\boldsymbol{Y}$	30.46	30.71	29.58	Same as Rot. $\boldsymbol{X}$ mode.	Logarithmic decrement.
Rot. $\boldsymbol{Z}$	30.46	30.17	29.10	Same as Rot. $\boldsymbol{X}$ mode.	Logarithmic decrement

- Hence, all the desired dynamically isotropic design variables can be obtained from this approach with input variables (a and f), known number of legs in each set (n_1 and n_2), and known payload variables Q, K, and h_c.

7 Experimental validation

This section validates the proposed analytical and FE-based dynamic model through experimental testing on a prototype of $\langle 3,\ 3\rangle$ dynamically isotropic TRGSP. The experimental setup for dynamically isotropic TRGSPs with more than six legs is planned for future work. For now, we validate our approach using data from our previously developed dynamically isotropic $\langle 3,\ 3\rangle$ TRGSP [111] that was designed for spacecraft micro-vibration isolation applications and tested with a dummy reaction wheel payload at UR Rao Satellite Center, Indian Space Research Organization (ISRO), Bangalore. The prototype carried a total payload mass of 10.37 kg (wheel plus platform), and the leg stiffness was approximately $k = 1.9 \times 10^5$ N/m as shown in Fig. 8(a).

The comparison of analytical (theoretical), FEM simulations, and experimental measurements of natural frequencies is presented in Table 5, along with the corresponding test setups. The results show good agreement across the first six modes, with experimental natural frequencies closely matching both the FEM and analytical values, and all discrepancies lying within the expected tolerance arising from manufacturing and material variations. Similarly, the damping for the first six modes was found to be around 4 % for the first six modes using all approaches. The damping ratios for the translational modes were estimated using the half-power bandwidth method applied to the frequency response functions obtained through Fast Fourier Transform (FFT). It is known that the finite frequency resolution associated with FFT-based spectral estimation can lead to a slight overestimation of damping for lightly damped systems. This explains the small difference observed between the damping values obtained for the translational modes (using the half-power bandwidth method) and those obtained for the rotational modes using the logarithmic decrement method. Despite this methodological difference, the estimated damping values remain close to each other, supporting the conclusion that the dynamically isotropic configuration distributes damping nearly uniformly across the modes.

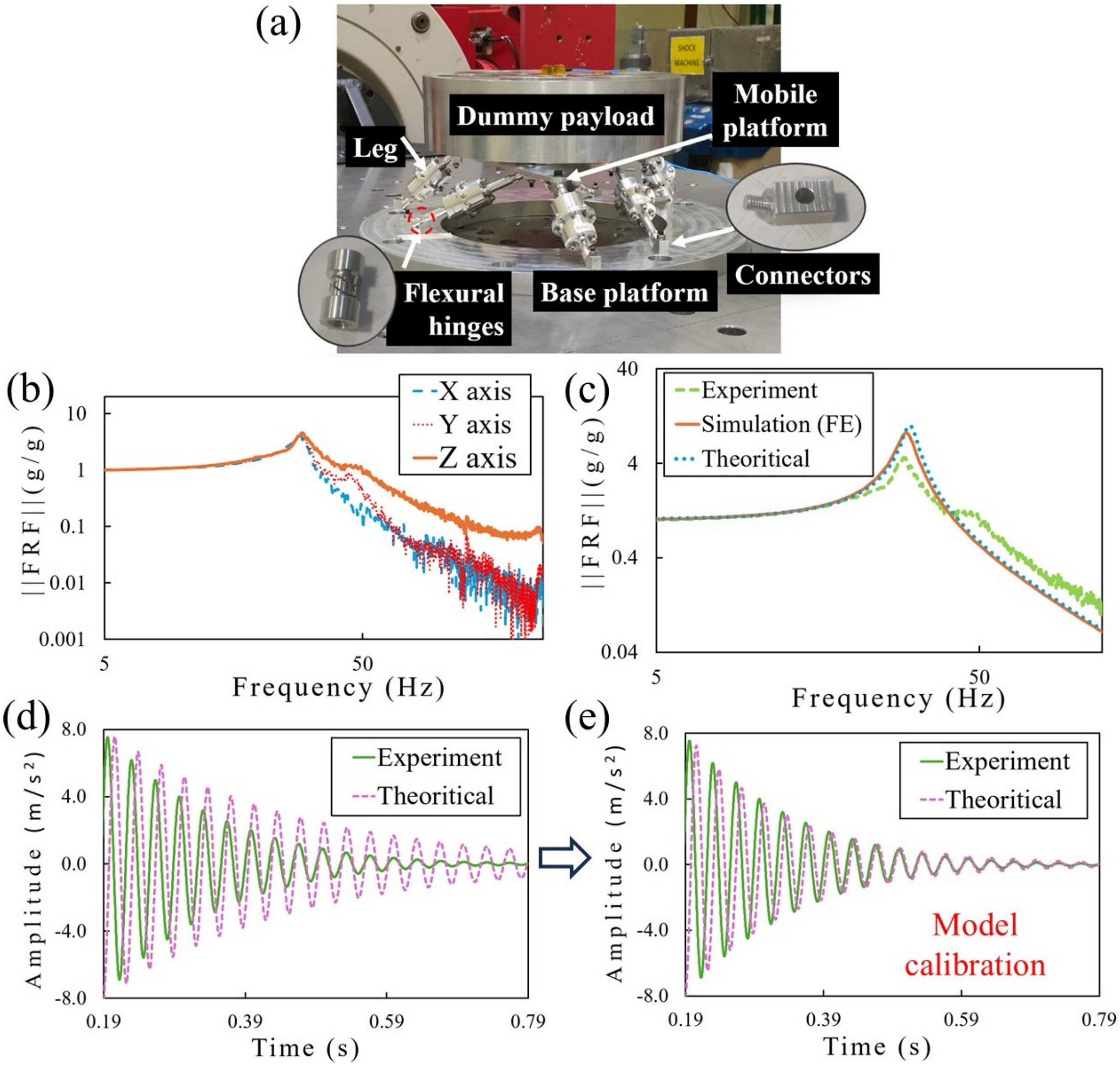

Figure 8: (a) Prototype of $\langle 3,\ 3\rangle$ dynamically isotropic TRGSP, (b) Experimental FRF curves for the $\boldsymbol{X}$, $\boldsymbol{Y}$, and $\boldsymbol{Z}$ modes, (c) Comparison of the FRF curve for $\boldsymbol{Z}$ mode for analytical, FEM, and experimental results for the $\langle 3,\ 3\rangle$ TRGSP, (d) Dynamic response for Rot($\boldsymbol{X}$) mode before model calibration, (e) Dynamic response for Rot($\boldsymbol{X}$) mode after model calibration.

The experimental FRF plots for the $\boldsymbol{X}$, $\boldsymbol{Y}$, and $\boldsymbol{Z}$ modes are shown in Fig. 8(b), where the natural frequency peaks appear at the same place. In the isolation region, the $\boldsymbol{X}$, $\boldsymbol{Y}$, and $\boldsymbol{Z}$ curves show slight differences in slope, which can be attributed to variations in modal participation mass between the lateral and longitudinal modes. On the other hand, the analytical and FEM results assume equal mass participation through a lumped mass model, leading to overlapping curves. Figure 8(c) presents a comparison of the analytical, FEM, and experimental results for one of the modes ($\boldsymbol{Z}$ mode) in a dynamically isotropic TRGSP – A similar trend is observed in other modes too. The local modes of the legs and platform were kept sufficiently high so that they don't interfere with the working range in the region of isolation. The phase differences observed between the experimental and predicted FRFs are primarily attributed to measurement uncertainties, sensor alignment errors, and structural compliance effects that are not fully captured in the analytical model. These factors tend to influence the phase response more significantly than the amplitude response in experimental modal measurements. Despite these small phase discrepancies, the measured amplitudes and natural frequencies show good agreement with the analytical and FEM results.

This confirms that our general framework, when applied with $n_1 = 3$ and $n_2 = 3$, converges to the same results for the $\langle 3,\ 3\rangle$ TRGSP prototype response and hence, validates our approach.

The performance of the proposed dynamically isotropic TRGSP can be compared with the well-known cubic GSP isolator with voice-coil actuation (active control) developed at ULB [23]. From the transmissibility curves reported in [23], the isolation-region slope is approximately 14 dB/octave without control and about 12 dB/octave with active control. In comparison, the present dynamically isotropic TRGSP achieves comparable isolation characteristics while operating purely as a passive system. Furthermore, the peak transmissibility reported in [23] is reduced from approximately 23 dB (without control) to about 5 dB with active control. This peak value is comparable to that observed in the present passive dynamically isotropic TRGSP, indicating similar behavior in the low-frequency amplification region. These results highlight that the proposed dynamically isotropic design can achieve competitive vibration isolation performance while avoiding the additional mass, power, and computational requirements associated with active control systems. It is worth noting that although the referenced system employs active control, its isolation performance is comparable to that of the proposed passive dynamically isotropic TRGSP. This is largely due to the relatively large spread in natural frequencies, characterized by a DII of 2.2 in this referenced system, indicating a non–dynamically isotropic design. Consequently, the resonance peaks associated with one DOF influence the isolation region of the other cross-DOF. This observation highlights the importance of achieving dynamic isotropy in multi-axis vibration isolation systems.

7.1 Model calibration

Although the analytical, FEM, and experimental results demonstrate close agreement, small discrepancies were observed in our prototype — typically within 0.5–1 Hz in natural frequency and around 1-2 % in damping ratio. These differences come from a few assumptions in the analytical formulation, such as neglecting the mass and inertia of the legs, assuming purely axial stiffness (no bending), and using perfectly symmetric payload properties. In actual practice, each leg in the prototype has a non-negligible mass of approximately 100–110 g (though small as compared to a 10.37 Kg payload), and the flexural joints used introduce a bending effect. The difference in peak across analytical, FE, and experimental results in 8(c) is due to differences in damping; for instance, damping due to friction at joints is only reflected in the experimental results. Hence, its damping value determined experimentally can be used for model calibration.

To refine the correlation between the analytical, FE, and experimental measurements, a model calibration process was performed. Parameters that significantly influence modal behavior and can be experimentally quantified (like damping) were iteratively adjusted in the analytical and FEM models. In addition to damping, the masses of the top platform and the legs were incorporated in the model. A sensitivity analysis carried out later in Section 7.2.2 for the strut masses shows that a leg mass of approximately 110 grams has a negligible influence on the dynamic isotropy of the system. Moreover, since the model includes flexural joints, the effect of bending compliance of the legs is inherently accounted for in the formulation. In contrast, parameters such as payload mass and inertia, geometric design variables (radius, angles, and height), and the number and arrangement of legs (n_1, n_2) were not altered during calibration.

The calibration process reduced the discrepancy in the dynamic response of each mode, and Figures 8(d) and 8(e) illustrate a representative comparison of the rotational $\boldsymbol{X}$ mode before and after calibration, showing greatly improved alignment. A similar trend is observed for other modes as well. This confirms that the analytical closed-form model remains highly accurate, provided that damping effects, mass and other parameters are appropriately incorporated. The overall calibration process adopted in this study is summarized in Fig. 10(b), which outlines the steps from analytical design to experimental comparison and parameter adjustment.

Overall, the strong agreement across analytical, FEM, and experimental results confirms the accuracy and practical implementability of the proposed dynamically isotropic TRGSP design methodology.

7.2 Sensitivity Analysis

To evaluate the robustness of the proposed dynamically isotropic design, a sensitivity analysis is performed by perturbing the key geometric parameters and the leg's mass around their nominal values. The objective is to examine how such deviations influence the Dynamic Isotropy Index (DII) and determine whether the system maintains near-isotropic behavior under practical design variations.

Table 6: Sensitivity analysis for dynamically isotropic MGSP in the FE model

	−20%	−10%	Actual	10%	20%
H	1.278	1.128	1.028	1.122	1.217
h_c	1.114	1.055	1.028	1.059	1.118
R_{to}	1.602	1.277	1.028	1.254	1.574
R_{bi}	1.141	1.078	1.028	1.044	1.077
α_{bi}	1.245	1.103	1.028	1.099	1.195
α_{to}	1.136	1.076	1.028	1.037	1.086

7.2.1 With dynamically isotropic parameters

While the parameters derived from our analytical geometry-based approach can be accurately modeled using finite element (FE) tools, real-world applications inevitably involve small deviations during hardware realization and manufacturing processes. It is essential to ensure that these deviations do not significantly compromise the MGSP's dynamic isotropy, keeping the DII below a threshold (typically DII=1.1). A sensitivity analysis was conducted in the FE model (design parameters corresponding to the $\langle 3,\ 3\rangle$ TRGSP prototype with a conventional joint type model) by varying parameters by ±20%, which showed that any deviations from the nominal values tend to increase the DII, as illustrated in Table 6. The observed trend is approximately linear in most cases. We conclude that for deviations of up to ±10% for most of the parameters, the DII remains around 1.1, which is acceptable. Therefore, our dynamically isotropic design demonstrates resilience to small design variations without significantly affecting its DII.

7.2.2 Incorporating mass/inertia in legs

In the FE analysis above, the strut masses were not considered. However, it is crucial to ensure that incorporating strut masses does not significantly impact the system's dynamic isotropy. In our hardware setup, each strut weighs approximately 120 grams, while the payload is 10 kg, resulting in a strut-to-payload mass ratio of about 0.012. When incorporating a 120-gram strut mass into the FE model, DII slightly increases to 1.031 from 1.028 for massless struts, and the frequency bandwidth decreases marginally from 29.76-30.60 Hz to 29.38-30.29 Hz.

Further analysis shows that increasing the strut-to-payload mass ratio to approximately 0.1 (with each strut weighing 1 kg) results in a DII of 1.1, a frequency bandwidth of 26.13-28.77 Hz. Therefore, our TRGSP design can maintain near dynamic isotropy, even with the inclusion of strut masses, without significantly affecting its vibration isolation performance.

8 Conclusions

This work presented a novel geometry-based analytical framework for the design of dynamically isotropic two-radii Gough–Stewart platforms (TRGSPs) with arbitrary number of legs capable of achieving uniform natural frequencies and damping across the first six degrees of freedom. Unlike conventional GSPs, which exhibit modal coupling and different natural frequency across the first six modes, the proposed TRGSP architecture enables dynamic isotropy. In a dynamically isotropic TRGSP, the natural frequencies for the first six modes are equal, allowing modes to be decoupled and tuned identically. This significantly simplifies controller design and improves passive vibration isolation performance, as the dampers can be easily tuned to a specific frequency bandwidth in a dynamically isotropic configuration.

Closed-form analytical solutions for the design variables were derived using a novel geometry-based approach that reduced a complex 3D TRGSP dynamic isotropic problem to a 2D geometric construction based on a pair of triangles. These solutions for the design variable in their explicit form provide a direct, and intuitive pathway to determine feasible and practical design parameters under geometric constraints with an arbitrary number of legs and payload properties. The proposed formulation is applicable to both even-and odd-legged TRGSP configurations. Closed-form expressions for the dynamically isotropic natural frequency, modal decoupling, and damping characteristics were derived for the dynamically isotropic TRGSPs. It was also shown that, when the two leg sets contain an equal number of legs, the resulting design parameters remain invariant with respect to the number of legs in each set. Later a novel transitional design strategy was also introduced when the payload requirement is enhanced, enabling cost-effective upgradation of existing platforms by simply adding legs rather than redesigning the entire system to accommodate the updated payload.

Under the stated modelling assumptions, i.e., same stiffness and equivalent damping in each leg, negligible mass of each leg, and axisymmetric paylaod, the proposed design approach was validated across various dynamic isotropic configurations in six-, seven- and eight-legged TRGSP through FEM simulations, demonstrating close agreement in natural frequencies, damping characteristics, and decoupling behaviour. While development of a multi-legged prototype is planned for the future, experimental validation was performed using a $\langle 3, 3\rangle$ TRGSP prototype, where the measured frequency response functions showed good agreement with the analytical and FEM predictions. The observed discrepancies between analytical, FEM and experimental responses were addressed through model calibration. A sensitivity analysis was also performed to evaluate the influence of key physical parameters such as leg mass and geometric variations on dynamic isotropy, demonstrating that the proposed TRGSP design remains robust to slight parameter deviations. In addition, the vibration-isolation performance of our $\langle 3, 3\rangle$ dynamically isotropic TRGSP protype was compared with a representative state-of-the-art GSP-based isolator, demonstrating that comparable isolation characteristics can be achieved while operating purely as a passive system.

Future work will focus on (i) fabrication and testing of dynamically isotropic TRGSPs with more than six legs, including odd-legged TRGSP configurations, and (ii) integration of passive, active, and hybrid damping strategies within the leg system and evaluation of their damping performance in a dynamically isotropic TRGSP with an arbitrary number of legs. Overall, the proposed framework establishes a foundation for next-generation multi-axis vibration isolation systems.

A Background on Dynamic Isotropy

This appendix provides additional background on modal coupling in multi-axis vibration isolation systems and explains the motivation for achieving dynamic isotropy in Gough–Stewart platforms. Isotropy refers to the homogeneous behavior of certain kinetostatic properties exhibited by a robot across all directions within its workspace [104]. Salisbury and Craig [118] were the first to introduce the concept of robot isotropy in 1982, focusing on manipulator hands with serial kinematics. Over the years, significant research efforts have delved into GSPs, encompassing design and control aspects, such as geometry orthogonality [34, 113, 119, 120, 121], kinematic isotropy [99, 100, 101, 102], stiffness isotropy [103] and static isotropy [87, 104, 105]. In the context of vibration isolation applications, the first six modes (three translational and three rotational modes) typically contain the majority of vibrational energy. For an efficient vibration isolation system, equal attenuation across the first six modes is imperative.

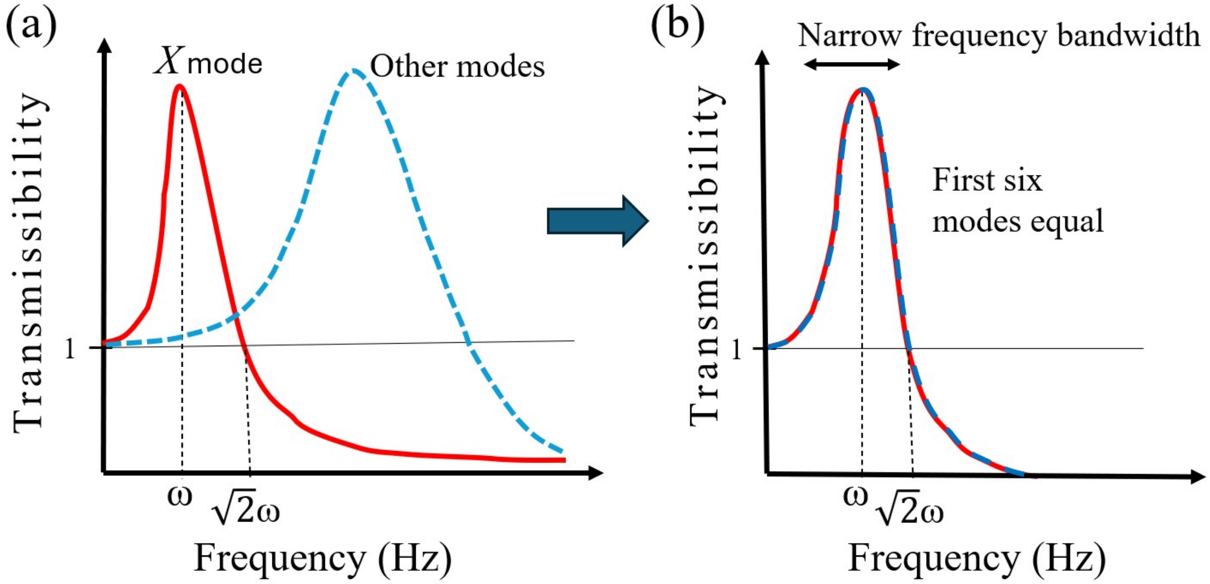

Figure 9: (a) The natural frequency peaks of all the modes are different, and the region of isolation for mode $\boldsymbol{X}$ is affected by resonance peaks of other modes. (b) Dynamic isotropy condition– the natural frequencies corresponding to the first six degrees of freedom are aligned, leading to effective vibration isolation.

Coupling between modes remains a major obstacle for multi-axis vibration isolation applications. Different natural frequency peaks of the six modes could affect isolator performance due to coupling [122] of the cross DOFs as depicted schematically in Fig. 9 – the usable isolation range (say, of the optical payload) of the $\boldsymbol{X}$ mode (typically beyond $\sqrt{2}\,\omega$ [70, 123]) in Fig. 9(a) is affected by peaks of the cross rotational or translational modes. For effective isolation of all the first six modes, it is ideal if the resonance peaks of the first six modes are aligned as shown in Fig. 9(b), as no mode interferes with other modes. This condition is termed "dynamic isotropy," where the first six natural frequencies are nearly equal, resulting in effective vibration isolation.

While kinematic or static isotropy in GSPs is advantageous for precise pointing applications [95], it proves less suitable for passive vibration isolation. This is because the resonance peaks of the first six natural frequencies are not aligned in these isotropies. For instance, the kinematically isotropic GSP designed for precise pointing features six distinct natural frequencies: 80.4, 80.4, 80.4, 50.8, 50.8, and 35.9 Hz [95]. Consequently, the isolation region corresponding to the lowest natural frequency (35.9 Hz) is compromised by the resonance peaks of the higher natural frequency modes.

B Supporting Mathematical Expressions for TRGSP for $h_c = 0$

This appendix provides the detailed mathematical expressions used in Sections 3 for deriving the dynamic isotropy conditions of a $\langle n_1, n_2 \rangle$ TRGSP. The complete symbolic forms of the diagonal terms λ_i and coupling (non-diagonal) terms μ_{ij} in the natural frequency matrix $[\mathbf{G}]$, together with the full expressions of the two leg lengths l_{out} and l_{in}, are presented here for completeness. These formulations are omitted from the main text to improve clarity and readability. For Section 3, the value of all $\lambda's$ and $\mu's$ in Eq. (4) are given as:

$$\lambda_1 = \lambda_2 = \frac{3k\ \left(n_2\ l_{out}^2 \Psi_1 + n_1\ l_{in}^2 \Psi_2\right)}{\left(2 m_p l_{out}^2 l_{in}^2\right)}, \quad \lambda_3 = \frac{3kH^2\left(n_2\ l_{out}^2 +\ n_1\ l_{in}^2\right)}{\left(m_p l_{out}^2 l_{in}^2\right)},$$

$$\lambda_4 = \frac{3k\Psi_5 H^2}{\left(2 I_{xx} l_{out}^2 l_{in}^2\right)}, \quad \lambda_5 = \lambda_4 \frac{(I_{xx})}{(I_{yy})}, \quad \lambda_6 = \frac{3k\left(n_2\ \Psi_6^2\ l_{out}^2 +\ n_1\ \Psi_7^2\ l_{in}^2\right)}{\left(I_{zz} l_{out}^2 l_{in}^2\right)},$$

$$\mu_{11} = \frac{-3kH\left(-n_2\ \Psi_6 l_{out}^2 +\ n_1\ \Psi_7 l_{in}^2\right)}{\left(2 l_{out}^2 l_{in}^2\right)}, \quad \mu_{33} = -2\mu_{11},$$

$$\mu_{12} = \frac{3kH\left(n_2\ \Psi_3 l_{out}^2 + n_1\ \Psi_4 l_{in}^2\right)}{\left(2 l_{out}^2 l_{in}^2\right)}.$$

where,

$$\Psi_1 = R_{ti}^2 +\ R_{bi}^2 - 2R_{ti}R_{bi}\cos\left(\alpha_{bi} - \alpha_{ti}\right)$$

$$\Psi_2 = R_{to}^2 +\ R_{bo}^2 - 2R_{to}R_{bo}\cos\left(\alpha_{to}\right)$$

$$\Psi_3 = R_{ti}^2 - R_{ti}R_{bi}\cos\left(\alpha_{bi} - \alpha_{ti}\right), \quad \Psi_4 = R_{to}^2 - R_{to}R_{bo}\cos\left(\alpha_{to}\right)$$

$$\Psi_5 = n_2\ R_{ti}^2 l_{out}^2 +\ n_1\ R_{to}^2 l_{in}^2, \quad \Psi_6 = R_{ti}R_{bi}\sin\left(\alpha_{bi} - \alpha_{ti}\right), \quad \Psi_7 = R_{to}R_{bo}\sin\left(\alpha_{to}\right).$$

As stated, $\langle n_1,\ n_2\rangle$ TRGSP has two sets of legs with lengths given by:

For the first set of legs, $l_{out} = |\boldsymbol{S_p}| = \left(\sqrt{R_{to}^2 + R_{bo}^2 - 2R_{to}R_{bo}\cos\left(\alpha_{to}\right) + H^2}\right)$ and similarly, $l_{in} = |\boldsymbol{S_j}| = \left(\sqrt{R_{ti}^2 + R_{bi}^2 - 2R_{ti}R_{bi}\cos\left(\alpha_{bi} - \alpha_{ti}\right) + H^2}\right)$, where, $1 \leq p \leq n_1$, and $n_1 + 1 \leq j \leq n_1 + n_2$.

The eigenvalue condition given in Eq. (6) thus leads to a set of transcendental equations, making it challenging to solve them in closed form. Our geometry-based approach, presented in Section 3.1, simplifies the problem through geometrical observation and facilitates a closed-form solution.

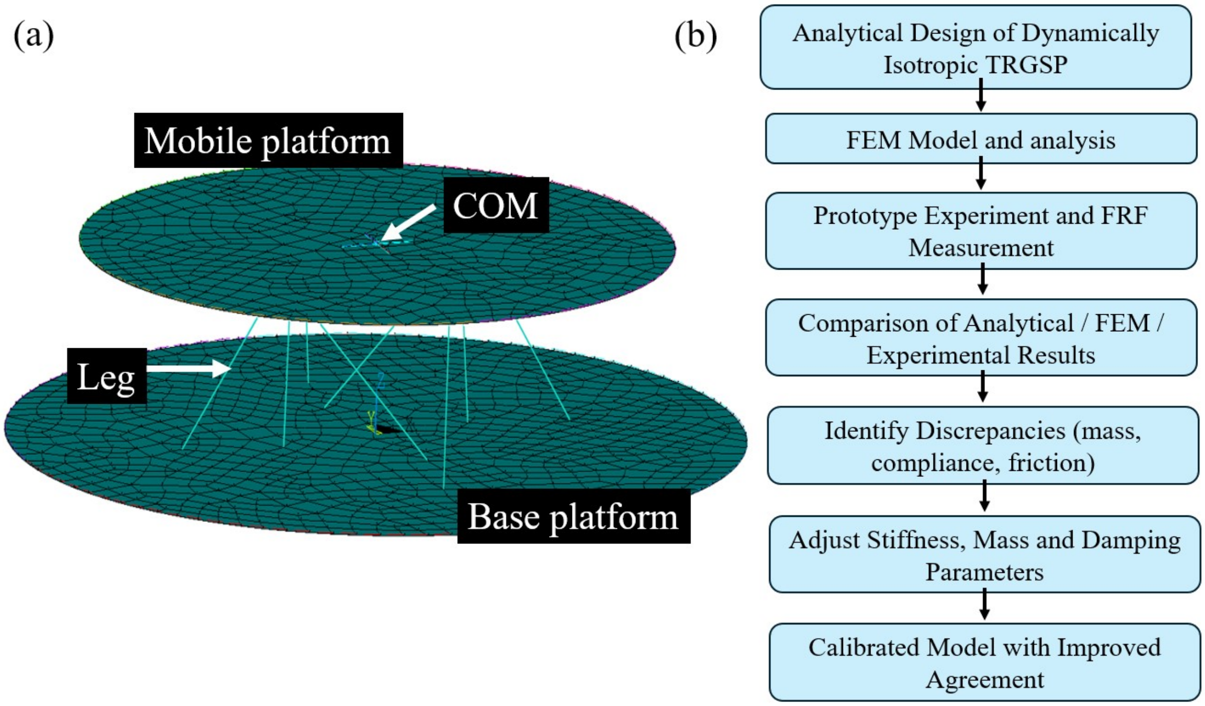

Figure 10: (a) FEM model of $\langle 4,\ 4\rangle$ dynamically isotropic TRGSP with eight legs created in ANSYS® to validate the analytical results; (b) Flowchart of the model calibration procedure showing the steps from analytical design to FEM verification, experimental comparison, and parameter adjustment.

C Finite Element Modelling Details

A finite element model of the TRGSP was created in ANSYS® in Section 5 to verify the appropriateness of our assumptions and analytical model in Section 3. The modeling assumptions and element types were chosen to closely match the conditions used in analytical derivations.

- The top and bottom platforms were modeled as rigid bodies using Shell181 elements.

- Each leg was represented as an ideal axial spring using Link180 elements to match the analytical stiffness assumption. The legs have no mass and inertia.
- The payload was modeled as a lumped mass with mass and inertia properties at its center of mass. The multi-point constraint (MPC) beam was used to fix the payload (lumped mass) with the mobile platform.
- The model was analysed about the neutral configurations, assuming small displacement characteristics. Since our focus is on the dynamic frequency response of the platform, the Coriolis, centripetal, gravitational, and other nonlinear terms are assumed to be negligible in this analysis [93].

The FE model created is shown in Fig. 10(a) and results from FE analysis are presented in detail in Section 5.

References

[1] W. Zhang, J. Che, H. Shu, Y. Bai, X. Liu, W. Jiang, J. Wu, X. Chen, Dynamic modeling and vibration characteristics analysis of parallel antenna, Mechanism and Machine Theory (2025) 106153`doi:10.1016/j.mechmachtheory.2025.106153`.

[2] W. XING, W. TUO, X. LI, T. WANG, C. YANG, Micro-vibration suppression and compensation techniques for in-orbit satellite: A review, Chinese Journal of Aeronautics 37 (9) (2024) 1–19. `doi:10.1016/j.cja.2024.05.036`.
URL `http://dx.doi.org/10.1016/j.cja.2024.05.036`

[3] Y. Lou, H. Zhang, L. Zhang, H. Cai, Advancements in key technologies for vibration isolators utilizing electromagnetic levitation, Energies 17 (21) (2024) 5343. `doi:10.3390/en17215343`.
URL `http://dx.doi.org/10.3390/en17215343`

[4] L. Li, L. Tan, L. Kong, D. Wang, H. Yang, The influence of flywheel micro vibration on space camera and vibration suppression, Mechanical Systems and Signal Processing 100 (2018) 360–370. `doi:10.1016/j.ymssp.2017.07.029`.
URL `http://dx.doi.org/10.1016/j.ymssp.2017.07.029`

[5] H. Yun, L. Liu, Q. Li, H. Yang, Investigation on two-stage vibration suppression and precision pointing for space optical payloads, Aerospace Science and Technology 96 (2020) 105543. `doi:10.1016/j.ast.2019.105543`.
URL `http://dx.doi.org/10.1016/j.ast.2019.105543`

[6] A. Stabile, V. V. Yotov, G. S. Aglietti, P. De Francesco, G. Richardson, Effect of boundary conditions on a high-performance isolation hexapod platform, Mechanism and Machine Theory 177 (2022) 105020. `doi:10.1016/j.mechmachtheory.2022.105020`.
URL `http://dx.doi.org/10.1016/j.mechmachtheory.2022.105020`

[7] E. Anderson, J. Fumo, R. Erwin, Satellite ultraquiet isolation technology experiment (suite), in: 2000 IEEE Aerospace Conference. Proceedings (Cat. No.00TH8484), AERO-00, IEEE. `doi:10.1109/aero.2000.878441`.
URL `http://dx.doi.org/10.1109/AERO.2000.878441`

[8] Y. Zhang, X. Guan, Active damping control of flexible appendages for spacecraft, Aerospace Science and Technology 75 (2018) 237–244. `doi:10.1016/j.ast.2017.12.027`.
URL `http://dx.doi.org/10.1016/j.ast.2017.12.027`

[9] Y. Cao, D. Cao, J. Wei, W. Huang, Modeling for solar array drive assembly system and compensating for the rotating speed fluctuation, Aerospace Science and Technology 84 (2019) 131–142. `doi:10.1016/j.ast.2018.10.028`.
URL `http://dx.doi.org/10.1016/j.ast.2018.10.028`

[10] J. Guo, Y. Geng, B. Wu, X. Kong, Vibration suppression of flexible spacecraft during attitude maneuver using cmgs, Aerospace Science and Technology 72 (2018) 183–192. `doi:10.1016/j.ast.2017.11.005`.
URL `http://dx.doi.org/10.1016/j.ast.2017.11.005`

[11] J.-M. L. Duigou, Microvibration measurements on SPOT 4, results of the micromedy experiment, Spacecraft Structures, Materials and Mechanical Testing 428 (1999) 475–483.

[12] L. Du, Y. Luo, L. Ji, F. Yang, Y. Zhang, S. Xie, Comprehensive parametric model and decoupling design of a Stewart platform for a large spaceborne optical load, Acta Astronautica 226 (2025) 119–134. `doi:10.1016/j.actaastro.2024.11.036`.
URL `http://dx.doi.org/10.1016/j.actaastro.2024.11.036`

[13] M. D. Lallo, Experience with the hubble space telescope: 20 years of an archetype, Optical Engineering 51 (1) (2012) 011011. `doi:10.1117/1.oe.51.1.011011`.
URL `http://dx.doi.org/10.1117/1.OE.51.1.011011`

[14] J. P. Gardner, J. C. Mather, M. Clampin, R. Doyon, M. A. Greenhouse, H. B. Hammel, J. B. Hutchings, P. Jakobsen, S. J. Lilly, K. S. Long, J. I. Lunine, M. J. Mccaughrean, M. Mountain,

J. Nella, G. H. Rieke, M. J. Rieke, H.-W. Rix, E. P. Smith, G. Sonneborn, M. Stiavelli, H. S. Stockman, R. A. Windhorst, G. S. Wright, The james webb space telescope, Space Science Reviews 123 (4) (2006) 485–606. `doi:10.1007/s11214-006-8315-7`.
URL `http://dx.doi.org/10.1007/s11214-006-8315-7`

[15] D. Stewart, A platform with six degrees of freedom, Proceedings of the Institution of Mechanical Engineers 180 (1) (1965) 371–386. `doi:10.1243/pime_proc_1965_180_029_02`.
URL `http://dx.doi.org/10.1243/PIME_PROC_1965_180_029_02`

[16] Y. Wen, W. Li, S. Zhou, F. Gao, W. Chen, Robust sliding mode control with adaptive gravity estimation of ship-borne Stewart platform for wave compensation, Applied Ocean Research 148 (2024) 104004. `doi:10.1016/j.apor.2024.104004`.
URL `http://dx.doi.org/10.1016/j.apor.2024.104004`

[17] J. LI, W. LI, X. ZHANG, H. HUANG, Design optimization of a hexapod vibration isolation system for electro-optical payload, Chinese Journal of Aeronautics 37 (2) (2024) 330–342. `doi:10.1016/j.cja.2023.12.003`.
URL `http://dx.doi.org/10.1016/j.cja.2023.12.003`

[18] B. Chung, J.-K. Lee, T.-S. Song, D.-k. Song, J.-H. Han, Alternative Stewart platform configuration for the enhanced isolation of cmg-induced microvibration, International Journal of Aeronautical and Space Sciences 26 (4) (2025) 1649–1662. `doi:10.1007/s42405-024-00857-8`.
URL `http://dx.doi.org/10.1007/s42405-024-00857-8`

[19] B. Patra, A. Nag, S. Bandyopadhyay, Analytical determination of the optimal effective regular workspace of a 6-6 Stewart platform manipulator for a specified orientation workspace, Mechanism and Machine Theory 203 (2024) 105791. `doi:10.1016/j.mechmachtheory.2024.105791`.
URL `http://dx.doi.org/10.1016/j.mechmachtheory.2024.105791`

[20] T. Zhang, X. Gong, L. Zhang, Y. Yu, A new modeling approach for parameter design of Stewart vibration isolation system integrated into complex systems, Machines 10 (11) (2022) 1005. `doi:10.3390/machines10111005`.
URL `http://dx.doi.org/10.3390/machines10111005`

[21] Y. Wu, K. Yu, J. Jiao, R. Zhao, Dynamic modeling and robust nonlinear control of a six-dof active micro-vibration isolation manipulator with parameter uncertainties, Mechanism and Machine Theory 92 (2015) 407–435. `doi:10.1016/j.mechmachtheory.2015.06.008`.
URL `http://dx.doi.org/10.1016/j.mechmachtheory.2015.06.008`

[22] C. Liu, X. Jing, S. Daley, F. Li, Recent advances in micro-vibration isolation, Mechanical Systems and Signal Processing 56–57 (2015) 55–80. `doi:10.1016/j.ymssp.2014.10.007`.
URL `http://dx.doi.org/10.1016/j.ymssp.2014.10.007`

[23] A. Preumont, M. Horodinca, I. Romanescu, B. de Marneffe, M. Avraam, A. Deraemaeker, F. Bossens, A. Abu Hanieh, A six-axis single-stage active vibration isolator based on Stewart platform, Journal of Sound and Vibration 300 (3) (2007) 644–661. `doi:https://doi.org/10.1016/j.jsv.2006.07.050`.

[24] D.-O. Lee, G. Park, J.-H. Han, Hybrid isolation of micro vibrations induced by reaction wheels, Journal of Sound and Vibration 363 (2016) 1–17. `doi:10.1016/j.jsv.2015.10.023`.
URL `http://dx.doi.org/10.1016/j.jsv.2015.10.023`

[25] J. Spanos, Z. Rahman, G. Blackwood, A soft 6-axis active vibration isolator, in: Proceedings of 1995 American Control Conference - ACC'95, ACC-95, American Autom Control Council. `doi:10.1109/acc.1995.529280`.
URL `http://dx.doi.org/10.1109/ACC.1995.529280`

[26] X. Li, P. Zhao, X. Jing, X-Stewart mechanism for vibration isolation with nonlinear translational-to-rotational motion properties, International Journal of Mechanical Sciences (2025) 110596`doi:10.1016/j.ijmecsci.2025.110596`.

[27] R. B. A. Shyam, N. Ahmad, R. Ranganath, A. Ghosal, Design of a dynamically isotropic Stewart-Gough platform for passive micro-vibration isolation in spacecraft using optimization, Journal of Spacecraft Technology 30 (2) (2019) 1–8.

[28] N. Ahmad, Vibration mitigation in spacecraft components using Stewart platform and particle impact damping, PhD Thesis, Indian Institute of Science (2020).

[29] Y. Chen, C. Qin, H. Zhou, Z. Xu, A. Xu, H. Li, Damping characteristics of a novel bellows viscous damper, Sensors 24 (19) (2024) 6265. `doi:10.3390/s24196265`.
URL `http://dx.doi.org/10.3390/s24196265`

[30] A. Stabile, G. S. Aglietti, G. Richardson, G. Smet, Design and verification of a negative resistance electromagnetic shunt damper for spacecraft micro-vibration, Journal of Sound and Vibration 386 (2017) 38–49. `doi:10.1016/j.jsv.2016.09.024`.
URL `http://dx.doi.org/10.1016/j.jsv.2016.09.024`

[31] A. Stabile, G. S. Aglietti, G. Richardson, G. Smet, A 2-collinear-dof strut with embedded negative-resistance electromagnetic shunt dampers for spacecraft micro-vibration, Smart Materials and Structures 26 (4) (2017) 045031. `doi:10.1088/1361-665x/aa61e3`.
URL `http://dx.doi.org/10.1088/1361-665X/aa61e3`

[32] J. Tang, K. Zhao, Y. Li, D. Cao, Vibration suppression of optical payload based on parallel manipulator, Journal of Vibration Engineering & Technologies 12 (7) (2024) 7595–7609. `doi:10.1007/s42417-024-01314-2`.
URL `http://dx.doi.org/10.1007/s42417-024-01314-2`

[33] D. Thayer, M. Campbell, J. Vagners, A. von Flotow, Six-axis vibration isolation system using soft actuators and multiple sensors, Journal of Spacecraft and Rockets 39 (2) (2002) 206–212. `doi:10.2514/2.3821`.
URL `http://dx.doi.org/10.2514/2.3821`

[34] J. McInroy, J. O'Brien, G. Neat, Precise, fault-tolerant pointing using a Stewart platform, IEEE/ASME Transactions on Mechatronics 4 (1) (1999) 91–95. `doi:10.1109/3516.752089`.
URL `http://dx.doi.org/10.1109/3516.752089`

[35] G. K. Foshage, T. Davis, J. M. Sullivan, T. Hoffman, A. Das, Hybrid active/passive actuator for spacecraft vibration isolation and suppression, in: A. E. Hatheway (Ed.), Actuator Technology and Applications, SPIE, 1996. `doi:10.1117/12.259033`.
URL `http://dx.doi.org/10.1117/12.259033`

[36] C. Taranti, B. Agrawal, R. Cristi, An efficient algorithm for vibration suppression to meet pointing requirements of optical payloads, in: AIAA Guidance, Navigation, and Control Conference and Exhibit, American Institute of Aeronautics and Astronautics, 2001. `doi:10.2514/6.2001-4094`.
URL `http://dx.doi.org/10.2514/6.2001-4094`

[37] R. Lin, Y. Li, J. Qian, P. Cheng, X. Gao, W. Sun, Y. Hu, Q. Yuan, Design of a vibration isolation platform for atomic force microscope based on flexural structure, Precision Engineering 89 (2024) 113–120. `doi:10.1016/j.precisioneng.2024.06.007`.
URL `http://dx.doi.org/10.1016/j.precisioneng.2024.06.007`

[38] C. Wang, X. Xie, Y. Chen, Z. Zhang, Investigation on active vibration isolation of a Stewart platform with piezoelectric actuators, Journal of Sound and Vibration 383 (2016) 1–19. `doi:https://doi.org/10.1016/j.jsv.2016.07.021`.

[39] A. Defendini, L. H. Vaillon, F. Trouve, T. Rouze, B. Sanctorum, G. Griseri, P. Spanoudakis, M. von Alberti, Technology predevelopment for active control of vibration and very high accuracy pointing systems, 2000.
URL `https://api.semanticscholar.org/CorpusID:108740122`

[40] A. Abu Hanieh, A. Preumont, N. Loix, Piezoelectric Stewart platform for general purpose active damping interface and precision control, in: R. Harris (Ed.), 9th European Space Mechanisms and Tribology Symposium, Vol. 480 of ESA Special Publication, 2001, pp. 331–334.

[41] Z. Geng, L. Haynes, Six degree-of-freedom active vibration control using the Stewart platforms, IEEE Transactions on Control Systems Technology 2 (1) (1994) 45–53. `doi:10.1109/87.273110`.
URL `http://dx.doi.org/10.1109/87.273110`

[42] L. Ran, W. Zhou, J. He, J. Wu, Y. Wang, X. Gong, Mems air-damped isolator for dual-axis micromirrors: Broad-range frequency vibration isolation, Journal of Microelectromechanical Systems 34 (3) (2025) 260–267. `doi:10.1109/jmems.2025.3543166`.
URL `http://dx.doi.org/10.1109/JMEMS.2025.3543166`

[43] W. Shi, L. Li, H. Fu, C. Shui, Y. Wang, D. Wang, X. Li, B. Zhang, A novel 6-dof passive vibration isolation system for aviation optoelectronic turret and its impact analysis on optical systems imaging performance, Aerospace 12 (9) (2025) 778. `doi:10.3390/aerospace12090778`.
URL `http://dx.doi.org/10.3390/aerospace12090778`

[44] W. Dai, J. Yang, M. Wiercigroch, Vibration energy flow transmission in systems with coulomb friction, International Journal of Mechanical Sciences 214 (2022) 106932. `doi:10.1016/j.ijmecsci.2021.106932`.
URL `http://dx.doi.org/10.1016/j.ijmecsci.2021.106932`

[45] D. Pietrosanti, M. De Angelis, A. Giaralis, Experimental study and numerical modeling of nonlinear dynamic response of sdof system equipped with tuned mass damper inerter (tmdi) tested on shaking table under harmonic excitation, International Journal of Mechanical Sciences 184 (2020) 105762. `doi:10.1016/j.ijmecsci.2020.105762`.
URL `http://dx.doi.org/10.1016/j.ijmecsci.2020.105762`

[46] L. Zhang, R. Zhang, L. Xie, S. Xue, Dynamics and isolation performance of a vibration isolator with a yoke-type nonlinear inerter, International Journal of Mechanical Sciences 254 (2023) 108447. `doi:10.1016/j.ijmecsci.2023.108447`.
URL `http://dx.doi.org/10.1016/j.ijmecsci.2023.108447`

[47] Y. Yu, F. Li, Low-frequency nonlinear vibration control of a dielectric elastomer-based semi-active system, Mechanical Systems and Signal Processing 234 (2025) 112878. `doi:10.1016/j.ymssp.2025.112878`.
URL `http://dx.doi.org/10.1016/j.ymssp.2025.112878`

[48] Z. Ma, R. Zhou, Q. Yang, H. P. Lee, K. Chai, A semi-active electromagnetic quasi-zero-stiffness vibration isolator, International Journal of Mechanical Sciences 252 (2023) 108357. `doi:10.1016/j.ijmecsci.2023.108357`.
URL `http://dx.doi.org/10.1016/j.ijmecsci.2023.108357`

[49] C. Liu, X. Jing, F. Li, Vibration isolation using a hybrid lever-type isolation system with an x-shape supporting structure, International Journal of Mechanical Sciences 98 (2015) 169–177. `doi:10.1016/j.ijmecsci.2015.04.012`.
URL `http://dx.doi.org/10.1016/j.ijmecsci.2015.04.012`

[50] S. Xu, X. Liu, Y. Wang, Z. Sun, J. Wu, Y. Shi, Frequency shaping-based h_∞ control for active pneumatic vibration isolation with input voltage saturation, Mechanical Systems and Signal Processing 220 (2024) 111705. `doi:10.1016/j.ymssp.2024.111705`.
URL `http://dx.doi.org/10.1016/j.ymssp.2024.111705`

[51] C. Huang, Z. Lin, H. Tang, S. Shu, Q. Liu, A hybrid add-on damping strategy for self-stabilization nanopositioning system with high-static-low-dynamic stiffness property, IEEE Transactions on Industrial Electronics 72 (5) (2025) 5041–5050. `doi:10.1109/tie.2024.3463013`.
URL `http://dx.doi.org/10.1109/TIE.2024.3463013`

[52] A. Nourian, M. R. Ghazavi, M. T. Masouleh, Generalized kinematic solution of hyper redundant multi Gough–Stewart platform connected serially using deep reinforcement learning with time optimization, Mechanism and Machine Theory 218 (2025) 106260. `doi:10.1016/j.mechmachtheory.2025.106260`.
URL `http://dx.doi.org/10.1016/j.mechmachtheory.2025.106260`

[53] S. Xu, Y. Wang, Z. Sun, C. Wang, Y. Shi, A compound regulative pneumatic vibration isolator with quasi-zero stiffness mechanism for load variable instruments, IEEE Transactions on Instrumentation and Measurement 73 (2024) 1–10. `doi:10.1109/tim.2024.3417599`.
URL `http://dx.doi.org/10.1109/TIM.2024.3417599`

[54] H. Hong, W. Kim, W. Kim, J.-m. Jeong, S. Kim, S. S. Kim, Machine learning-driven design optimization of buckling-induced quasi-zero stiffness metastructures for low-frequency vibration isolation,

ACS Applied Materials Interfaces 16 (14) (2024) 17965–17972. doi:10.1021/acsami.3c18793.
URL http://dx.doi.org/10.1021/acsami.3c18793

[55] Y. Li, Z. Wu, Y. Peng, S. Yao, J. Zhou, Full-band vibration isolation of multi-step quasi-zero stiffness systems, International Journal of Mechanical Sciences 274 (2024) 109277. doi:10.1016/j.ijmecsci.2024.109277.
URL http://dx.doi.org/10.1016/j.ijmecsci.2024.109277

[56] K. Yu, Y. Chen, C. Yu, J. Zhang, X. Lu, An origami-inspired low-frequency isolator with one/two-stage quasi-zero stiffness characteristics, International Journal of Mechanical Sciences 289 (2025) 110040. doi:10.1016/j.ijmecsci.2025.110040.
URL http://dx.doi.org/10.1016/j.ijmecsci.2025.110040

[57] S. Guo, S. Liu, R. Gao, A bidirectional quasi-zero stiffness metamaterial for impact attenuation, International Journal of Mechanical Sciences 268 (2024) 108998. doi:10.1016/j.ijmecsci.2024.108998.
URL http://dx.doi.org/10.1016/j.ijmecsci.2024.108998

[58] H. Wan, H. Chen, Y. Wang, X. Fang, Y. Liu, K. Kosiba, Laser additive manufacturing of miura-origami tube inspired quasi-zero stiffness metamaterial with prominent longitudinal wave propagation, Virtual and Physical Prototyping 19 (1) (Jan. 2024). doi:10.1080/17452759.2023.2299691.
URL http://dx.doi.org/10.1080/17452759.2023.2299691

[59] X. Liu, S. Chen, B. Wang, X. Tan, L. Yu, A compact quasi-zero-stiffness mechanical metamaterial based on truncated conical shells, International Journal of Mechanical Sciences 277 (2024) 109390. doi:10.1016/j.ijmecsci.2024.109390.
URL http://dx.doi.org/10.1016/j.ijmecsci.2024.109390

[60] T. Deng, G. Wen, H. Ding, Z.-Q. Lu, L.-Q. Chen, A bio-inspired isolator based on characteristics of quasi-zero stiffness and bird multi-layer neck, Mechanical Systems and Signal Processing 145 (2020) 106967. doi:10.1016/j.ymssp.2020.106967.
URL http://dx.doi.org/10.1016/j.ymssp.2020.106967

[61] Q. Zhu, K. Chai, Magnetic negative stiffness devices for vibration isolation systems: A state-of-the-art review from theoretical models to engineering applications, Applied Sciences 14 (11) (2024) 4698. doi:10.3390/app14114698.
URL http://dx.doi.org/10.3390/app14114698

[62] R. Zhou, Z. Huang, H. Chen, J. Wu, J. Che, X. Chen, W. Jiang, Inverse design method of magnetic springs with customized force–displacement relationship over a wide range, IEEE Transactions on Industrial Electronics 71 (8) (2024) 9394–9404. doi:10.1109/tie.2023.3319710.
URL http://dx.doi.org/10.1109/TIE.2023.3319710

[63] M. Wu, R. Gao, Y. Zhou, J. Che, J. Wu, X. Li, X. Chen, W. Jiang, Analysis and experiment of a multi-tile magnetic spring with high negative stiffness, Mechanical Systems and Signal Processing 223 (2025) 111914. doi:10.1016/j.ymssp.2024.111914.
URL http://dx.doi.org/10.1016/j.ymssp.2024.111914

[64] R. Gao, J. Che, M. Wu, W. Zhang, X. Xie, J. Wu, X. Chen, W. Jiang, Axial-offset magnetic negative stiffness spring with high density and linearity, International Journal of Mechanical Sciences 287 (2025) 109989. doi:10.1016/j.ijmecsci.2025.109989.
URL http://dx.doi.org/10.1016/j.ijmecsci.2025.109989

[65] X. Sun, S. Zhang, J. Xu, Parameter design of a multi-delayed isolator with asymmetrical nonlinearity, International Journal of Mechanical Sciences 138–139 (2018) 398–408. doi:10.1016/j.ijmecsci.2018.02.026.
URL http://dx.doi.org/10.1016/j.ijmecsci.2018.02.026

[66] J. Xu, X. Sun, A multi-directional vibration isolator based on quasi-zero-stiffness structure and time-delayed active control, International Journal of Mechanical Sciences 100 (2015) 126–135. doi:10.1016/j.ijmecsci.2015.06.015.
URL http://dx.doi.org/10.1016/j.ijmecsci.2015.06.015

[67] J. Zhao, G. Zhou, D. Zhang, I. Kovacic, R. Zhu, H. Hu, Integrated design of a lightweight metastructure for broadband vibration isolation, International Journal of Mechanical Sciences 244 (2023) 108069. doi:10.1016/j.ijmecsci.2022.108069.
URL http://dx.doi.org/10.1016/j.ijmecsci.2022.108069

[68] Z. Liu, Q. Lv, D. Li, R. Huan, Z. Huang, A straight-arch-straight beam tandem quasi-zero stiffness structure, International Journal of Mechanical Sciences 286 (2025) 109818. doi:10.1016/j.ijmecsci.2024.109818.
URL http://dx.doi.org/10.1016/j.ijmecsci.2024.109818

[69] T. D. Le, K. K. Ahn, Experimental investigation of a vibration isolation system using negative stiffness structure, International Journal of Mechanical Sciences 70 (2013) 99–112. doi:10.1016/j.ijmecsci.2013.02.009.
URL http://dx.doi.org/10.1016/j.ijmecsci.2013.02.009

[70] X. Sun, J. Xu, X. Jing, L. Cheng, Beneficial performance of a quasi-zero-stiffness vibration isolator with time-delayed active control, International Journal of Mechanical Sciences 82 (2014) 32–40. `doi:10.1016/j.ijmecsci.2014.03.002`.
URL `http://dx.doi.org/10.1016/j.ijmecsci.2014.03.002`

[71] D. L. Platus, Negative-stiffness-mechanism vibration isolation systems, in: C. G. Gordon (Ed.), Vibration Control in Microelectronics, Optics, and Metrology, SPIE, 1992. `doi:10.1117/12.56823`.
URL `http://dx.doi.org/10.1117/12.56823`

[72] R. Zeng, S. Yin, G. Wen, J. Zhou, A non-smooth quasi-zero-stiffness isolator with displacement constraints, International Journal of Mechanical Sciences 225 (2022) 107351. `doi:10.1016/j.ijmecsci.2022.107351`.
URL `http://dx.doi.org/10.1016/j.ijmecsci.2022.107351`

[73] K. Wang, J. Zhou, D. Xu, Sensitivity analysis of parametric errors on the performance of a torsion quasi-zero-stiffness vibration isolator, International Journal of Mechanical Sciences 134 (2017) 336–346. `doi:10.1016/j.ijmecsci.2017.10.026`.
URL `http://dx.doi.org/10.1016/j.ijmecsci.2017.10.026`

[74] B. Yan, H. Ma, C. Zhao, C. Wu, K. Wang, P. Wang, A vari-stiffness nonlinear isolator with magnetic effects: Theoretical modeling and experimental verification, International Journal of Mechanical Sciences 148 (2018) 745–755. `doi:10.1016/j.ijmecsci.2018.09.031`.
URL `http://dx.doi.org/10.1016/j.ijmecsci.2018.09.031`

[75] R.-B. Hao, Z.-Q. Lu, H. Ding, L.-Q. Chen, Orthogonal six-dofs vibration isolation with tunable high-static-low-dynamic stiffness: Experiment and analysis, International Journal of Mechanical Sciences 222 (2022) 107237. `doi:10.1016/j.ijmecsci.2022.107237`.
URL `http://dx.doi.org/10.1016/j.ijmecsci.2022.107237`

[76] Y. Yao, H. Li, Y. Li, X. Wang, Analytical and experimental investigation of a high-static-low-dynamic stiffness isolator with cam-roller-spring mechanism, International Journal of Mechanical Sciences 186 (2020) 105888. `doi:10.1016/j.ijmecsci.2020.105888`.
URL `http://dx.doi.org/10.1016/j.ijmecsci.2020.105888`

[77] F. Zhao, J. Ji, K. Ye, Q. Luo, An innovative quasi-zero stiffness isolator with three pairs of oblique springs, International Journal of Mechanical Sciences 192 (2021) 106093. `doi:10.1016/j.ijmecsci.2020.106093`.
URL `http://dx.doi.org/10.1016/j.ijmecsci.2020.106093`

[78] Q. Wang, J. Zhou, K. Wang, Q. Lin, D. Xu, G. Wen, A compact quasi-zero-stiffness device for vibration suppression and energy harvesting, International Journal of Mechanical Sciences 250 (2023) 108284. doi:10.1016/j.ijmecsci.2023.108284.
URL http://dx.doi.org/10.1016/j.ijmecsci.2023.108284

[79] A. Carrella, M. Brennan, T. Waters, V. Lopes, Force and displacement transmissibility of a nonlinear isolator with high-static-low-dynamic-stiffness, International Journal of Mechanical Sciences 55 (1) (2012) 22–29. doi:10.1016/j.ijmecsci.2011.11.012.
URL http://dx.doi.org/10.1016/j.ijmecsci.2011.11.012

[80] M. Li, W. Cheng, R. Xie, A quasi-zero-stiffness vibration isolator using a cam mechanism with user-defined profile, International Journal of Mechanical Sciences 189 (2021) 105938. doi:10.1016/j.ijmecsci.2020.105938.
URL http://dx.doi.org/10.1016/j.ijmecsci.2020.105938

[81] S. Zuo, D. Wang, Y. Zhang, Q. Luo, Design and testing of a parabolic cam-roller quasi-zero-stiffness vibration isolator, International Journal of Mechanical Sciences 220 (2022) 107146. doi:10.1016/j.ijmecsci.2022.107146.
URL http://dx.doi.org/10.1016/j.ijmecsci.2022.107146

[82] C. Zheng, J. Wu, J. Liu, X. Xue, Hysteresis dynamic modeling of 4-sps parallel all-metallic isolator with spherical joints considering nonlinear micro-collision and interfacial friction, Journal of Sound and Vibration 596 (2025) 118778. doi:10.1016/j.jsv.2024.118778.
URL http://dx.doi.org/10.1016/j.jsv.2024.118778

[83] A. Mishra, P. Ghosh, N. Tiwari, Design, development, and control of a 2pru-1prs stabilized platform, International Journal of Dynamics and Control 13 (7) (Jun. 2025). doi:10.1007/s40435-025-01769-5.
URL http://dx.doi.org/10.1007/s40435-025-01769-5

[84] B. Liao, Y. Xie, D. Zhou, Y. Zhu, H. Wei, Vibration transfer analysis of a 6-dof platform with oblique-mounted pyramid configuration and rigidly-hinged-mixed support, Measurement Science and Technology 36 (5) (2025) 055902. doi:10.1088/1361-6501/adcad6.
URL http://dx.doi.org/10.1088/1361-6501/adcad6

[85] V. L. Nguyen, L. Nurahmi, V.-T. Nguyen, Design of a low-frequency vibration isolator with large-stroke and variable-payload capabilities using gear-spring units, Journal of Mechanisms and Robotics 17 (10) (Jun. 2025). doi:10.1115/1.4068692.
URL http://dx.doi.org/10.1115/1.4068692

[86] Y. Hou, J. Yao, L. Lu, Y. Zhao, Performance analysis and comprehensive index optimization of a new configuration of Stewart six-component force sensor, Mechanism and Machine Theory 44 (2) (2009) 359–368. `doi:10.1016/j.mechmachtheory.2008.03.008`.
URL `http://dx.doi.org/10.1016/j.mechmachtheory.2008.03.008`

[87] S. Bandyopadhyay, A. Ghosal, An algebraic formulation of static isotropy and design of statically isotropic 6–6 Stewart platform manipulators, Mechanism and Machine Theory 44 (7) (2009) 1360–1370. `doi:10.1016/j.mechmachtheory.2008.11.002`.
URL `http://dx.doi.org/10.1016/j.mechmachtheory.2008.11.002`

[88] B. Afzali-Far, A. Andersson, K. Nilsson, P. Lidström, Dynamic isotropy in 6-dof kinematically constrained platforms by three elastic nodal joints, Precision Engineering 45 (2016) 342–358. `doi:10.1016/j.precisioneng.2016.03.011`.
URL `http://dx.doi.org/10.1016/j.precisioneng.2016.03.011`

[89] B. Afzali-Far, P. Lidström, Analytical index of dynamic isotropy and its application to hexapods, Precision Engineering 52 (2018) 242–248. `doi:http://dx.doi.org/10.1016/j.precisioneng.2018.01.001`.

[90] B. Afzali-Far, P. Lidström, A Class of Generalized Gough-Stewart Platforms Used for Effectively Obtaining Dynamic Isotropy – An Analytical Study, MATEC Web of Conferences 35 (2015) 02002:P.1–P.5. `doi:https://doi.org/10.1051/matecconf/20153502002`.

[91] H.-Z. Jiang, J.-F. He, Z.-Z. Tong, Characteristics analysis of joint space inverse mass matrix for the optimal design of a 6-dof parallel manipulator, Mechanism and Machine Theory 45 (5) (2010) 722–739. `doi:10.1016/j.mechmachtheory.2009.12.003`.
URL `http://dx.doi.org/10.1016/j.mechmachtheory.2009.12.003`

[92] H.-Z. Jiang, J.-f. He, Z.-Z. Tong, W. Wang, Dynamic isotropic design for modified Gough-Stewart platforms lying on a pair of circular hyperboloids, Mechanism and Machine Theory 46 (9) (2011) 1301–1315. `doi:https://doi.org/10.1016/j.mechmachtheory.2011.04.003`.

[93] H.-Z. Jiang, Z.-Z. Tong, J.-f. He, Dynamic isotropic design of a class of Gough-Stewart parallel manipulators lying on a circular hyperboloid of one sheet, Mechanism and Machine Theory 46 (3) (2011) 358–374. `doi:10.1016/j.mechmachtheory.2010.10.008`.

[94] Y. Pratap Singh, N. Ahmad, A. Ghosal, Design of decoupled and dynamically isotropic parallel manipulators considering five degrees-of-freedom, Journal of Mechanisms and Robotics 16 (1) (Apr.

2023). doi:10.1115/1.4062176.
URL http://dx.doi.org/10.1115/1.4062176

[95] H. Yun, L. Liu, Q. Li, W. Li, L. Tang, Development of an isotropic Stewart platform for telescope secondary mirror, Mechanical Systems and Signal Processing 127 (2019) 328–344. doi:https://doi.org/10.1016/j.ymssp.2019.03.001.

[96] Y. Wu, K. Yu, J. Jiao, D. Cao, W. Chi, J. Tang, Dynamic isotropy design and analysis of a six-dof active micro-vibration isolation manipulator on satellites, Robotics and Computer-Integrated Manufacturing 49 (2018) 408–425. doi:10.1016/j.rcim.2017.08.003.
URL http://dx.doi.org/10.1016/j.rcim.2017.08.003

[97] X. Yang, H. Wu, Y. Li, B. Chen, Dynamic isotropic design and decentralized active control of a six-axis vibration isolator via Stewart platform, Mechanism and Machine Theory 117 (2017) 244–252. doi:10.1016/j.mechmachtheory.2017.07.017.
URL http://dx.doi.org/10.1016/j.mechmachtheory.2017.07.017

[98] P. Mukherjee, B. Dasgupta, A. Mallik, Dynamic stability index and vibration analysis of a flexible Stewart platform, Journal of Sound and Vibration 307 (3–5) (2007) 495–512. doi:10.1016/j.jsv.2007.05.036.

[99] K. E. Zanganeh, J. Angeles, Kinematic isotropy and the optimum design of parallel manipulators, The International Journal of Robotics Research 16 (2) (1997) 185–197. doi:10.1177/027836499701600205.
URL http://dx.doi.org/10.1177/027836499701600205

[100] K. Tsai, K. Huang, The design of isotropic 6-dof parallel manipulators using isotropy generators, Mechanism and Machine Theory 38 (11) (2003) 1199–1214. doi:10.1016/S0094-114X(03)00067-3.
URL http://dx.doi.org/10.1016/S0094-114X(03)00067-3

[101] A. Fattah, A. M. H. Ghasemi, Isotropic design of spatial parallel manipulators, The International Journal of Robotics Research 21(9) (2002) 811–824. doi:https://doi.org/10.1177/027836490202100984.

[102] S. Bandyopadhyay, A. Ghosal, An algebraic formulation of kinematic isotropy and design of isotropic 6-6 Stewart platform manipulators, Mechanism and Machine Theory 43 (5) (2008) 591–616. doi:10.1016/j.mechmachtheory.2007.05.003.
URL http://dx.doi.org/10.1016/j.mechmachtheory.2007.05.003

[103] J. Zhenlin, G. Feng, Z. Xiaohui, Design and analysis of a novel isotropic six-component force/torque sensor, Sensors and Actuators A: Physical 109 (1–2) (2003) 17–20. doi:10.1016/S0924-4247(03)00299-1.
URL http://dx.doi.org/10.1016/S0924-4247(03)00299-1

[104] I. Fassi, G. Legnani, D. Tosi, Geometrical conditions for the design of partial or full isotropic hexapods, Journal of Robotic Systems 22 (10) (2005) 507–518. doi:10.1002/rob.20074.
URL http://dx.doi.org/10.1002/rob.20074

[105] J. Yao, Y. Hou, H. Wang, T. Zhou, Y. Zhao, Spatially isotropic configuration of Stewart platform-based force sensor, Mechanism and Machine Theory 46 (2) (2011) 142–155. doi:10.1016/j.mechmachtheory.2010.10.002.

[106] Z. Belabed, M. A. Kenanda, F. Hammadi, H. M. Sedighi, Shear-locking-free finite element formulation for vibrating functionally graded graphene nanocomposites using an enriched quadrilateral plate element, Engineering with Computers 41 (6) (2025) 4393–4415. doi:10.1007/s00366-025-02210-3.
URL http://dx.doi.org/10.1007/s00366-025-02210-3

[107] Z. Zhao, Y. Liu, C. Yu, P. Jiang, A fuzzy neural network approach for predicting and optimizing the dynamic stiffness of the stewart platform, Discover Computing 28 (1) (Nov. 2025). doi:10.1007/s10791-025-09786-w.
URL http://dx.doi.org/10.1007/s10791-025-09786-w

[108] M. Kenanda, F. Hammadi, H. Bahai, Z. Belabed, A new efficient nonlocal hyperbolic hsdt for mechanical vibration of porous fgm plates/nanoplates using navier's method and artificial neural network prediction, International Journal of Solids and Structures 325 (2026) 113719. doi:10.1016/j.ijsolstr.2025.113719.
URL http://dx.doi.org/10.1016/j.ijsolstr.2025.113719

[109] Z. Xia, Y. Xing, C. Tian, D. Zhang, Advances in generalized parallel mechanisms: Coupling, configurable, and articulated designs, Mechanism and Machine Theory 218 (2025) 106287. doi:10.1016/j.mechmachtheory.2025.106287.
URL http://dx.doi.org/10.1016/j.mechmachtheory.2025.106287

[110] Z. Tong, J. He, H. Jiang, G. Duan, Optimal design of a class of generalized symmetric Gough-Stewart parallel manipulators with dynamic isotropy and singularity-free workspace, Robotica 30 (2) (2012) 305–314. doi:https://doi.org/10.1017/S0263574711000531.

[111] Y. P. Singh, N. Ahmad, A. Ghosal, Dynamically isotropic Gough–Stewart platform for micro-vibration isolation in spacecrafts, Mechanism and Machine Theory 201 (2024) 105735. `doi:10.1016/j.mechmachtheory.2024.105735`.
URL `http://dx.doi.org/10.1016/j.mechmachtheory.2024.105735`

[112] A. A. Allais, J. E. McInroy, J. F. O'Brien, Locally decoupled micromanipulation using an even number of parallel force actuators, IEEE Transactions on Robotics 28 (6) (2012) 1323–1334. `doi:10.1109/TRO.2012.2209229`.
URL `http://dx.doi.org/10.1109/TRO.2012.2209229`

[113] Y. Yi, J. McInroy, F. Jafari, Generating classes of locally orthogonal Gough-Stewart platforms, IEEE Transactions on Robotics 21 (5) (2005) 812–820. `doi:10.1109/TRO.2005.851360`.
URL `http://dx.doi.org/10.1109/TRO.2005.851360`

[114] A.-m. Hui, Influence of geometric parameters on the shock characteristics of the Stewart mechanism with eight legs, Journal of Vibration Engineering & Technologies 13 (2025) 244. `doi:10.1007/s42417-025-01801-0`.

[115] J. L. Allen, Active rack isolation system (ARIS) users guide, NASA Johnson Space Center/Boeing, Houston, TX, Tech. Rep., SSP 57006 (1999).

[116] W. Zhang, X. Chen, Z. Hu, J. Tang, A novel parallel mechanism with an extra rod for shock isolation, Shock and Vibration 2023 (2023) 1–12. `doi:10.1155/2023/1612345`.

[117] H.-Z. Liu, X.-Z. Huang, M. Yan, M.-X. Chang, Dynamic response and time-variant reliability analysis of an eight-rod shock isolator, Proceedings of the Institution of Mechanical Engineers, Part C: Journal of Mechanical Engineering Science 236 (13) (2022) 7041–7054. `doi:10.1177/09544062211070464`.

[118] J. K. Salisbury, J. J. Craig, Articulated hands: Force control and kinematic issues, The International Journal of Robotics Research 1 (1) (1982) 4–17. `doi:10.1177/027836498200100102`.
URL `http://dx.doi.org/10.1177/027836498200100102`

[119] Y. Yi, J. McInroy, F. Jafari, Generating classes of orthogonal Gough-Stewart platforms, in: IEEE International Conference on Robotics and Automation, 2004. Proceedings. ICRA '04. 2004, IEEE, 2004. `doi:10.1109/robot.2004.1302505`.
URL `http://dx.doi.org/10.1109/ROBOT.2004.1302505`

[120] F. Jafari, J. McInroy, Orthogonal Gough-Stewart platforms for micromanipulation, IEEE Transactions on Robotics and Automation 19 (4) (2003) 595–603. `doi:10.1109/tra.2003.814506`.
URL `http://dx.doi.org/10.1109/TRA.2003.814506`

[121] Y. Yi, J. McInroy, Y. Chen, Fault tolerance of parallel manipulators using task space and kinematic redundancy, IEEE Transactions on Robotics 22 (5) (2006) 1017–1021. `doi:10.1109/tro.2006.878973`.
URL `http://dx.doi.org/10.1109/TRO.2006.878973`

[122] Z. Chong, F. Xie, X.-J. Liu, J. Wang, Evaluation of dynamic isotropy and coupling acceleration capacity for a parallel manipulator with mixed dofs, Mechanism and Machine Theory 163 (2021) 104382. `doi:10.1016/j.mechmachtheory.2021.104382`.
URL `http://dx.doi.org/10.1016/j.mechmachtheory.2021.104382`

[123] C. Liu, W. Zhang, K. Yu, T. Liu, Y. Zheng, Quasi-zero-stiffness vibration isolation: Designs, improvements and applications, Engineering Structures 301 (2024) 117282. `doi:10.1016/j.engstruct.2023.117282`.
URL `http://dx.doi.org/10.1016/j.engstruct.2023.117282`